

Kinetics of the reduction of 4-nitrophenol by silver nanoparticles immobilized in thermoresponsive core-shell nanoreactors

Daniel Besold, Sebastian Risse,* Yan Lu,§ Joachim Dzubiella† and Matthias Ballauff‡

Soft Matter and Functional Materials, Helmholtz-Zentrum Berlin für Materialien und Energie, Hahn-Meitner-Platz 1, 14109 Berlin, Germany

KEYWORDS: responsive nanoreactors, PNIPAM, 4-nitrophenol, nanocatalysis, kinetics, spectral decomposition, Levenberg-Marquardt algorithm

ABSTRACT: We present a kinetic study on the reduction of 4-nitrophenol (NO_2) with borohydride, catalyzed by silver nanoparticles. The latter are immobilized inside the hydrogel shell of core-shell nanoreactors, comprising a polystyrene core, surrounded by a thermoresponsive poly-*N*-isopropylacrylamide (PNIPAM) hydrogel shell. Cryogenic transmission electron microscopy shows that silver nanoparticles with an average diameter of 5.6 ± 2.4 nm are located deep inside the PNIPAM shell. The Levenberg-Marquardt-algorithm is applied for the decomposition of UV-Vis spectra, recorded during the reduction of NO_2 , and its potential use in the assessment and evaluation of model reactions is demonstrated. The decomposition of UV-Vis spectra, obtained in a wavelength range of 240 to 500 nm, shows that the reactant NO_2 is directly transferred to the product 4-aminophenol (NH_2) without accumulation of intermediates. Hence, a stationary state for the intermediate 4-hydroxylaminophenol is present from the beginning of the reaction onwards. Based on this, a kinetic model is presented, which is related to a model previously derived for the kinetic analysis of the reaction catalyzed by gold. The kinetic data, obtained at room temperature at nine different combinations of NO_2 and borohydride concentrations, are globally fitted by a genetic approach. The results are in good accordance with previous results obtained on gold and, furthermore, show that the adsorption of NH_2 to the catalyst surface has a substantial influence on the kinetics on silver. Measurements between $T = 10$ and 50 °C reveal a non-Arrhenius dependency of the reaction rate, caused by the thermoresponsive PNIPAM hydrogel. We show how a systematic decomposition of kinetic, adsorption and partitioning effects provides useful qualitative insights on the partitioning coefficients of reactants and products, i.e. the ratio of the concentration inside/outside the hydrogel network, which play a significant role in the kinetics of PNIPAM-based catalysts. Furthermore, it is found that small ions like chloride and borohydride show a similar partitioning behavior in PNIPAM.

Introduction

In today's context of the increasing challenges of becoming economically/energetically more efficient and the trend to "greener" (and more selective) chemical processes to protect the environment, novel approaches are emerging for rational catalyst design.¹⁻³ Here, metallic nanoparticles have become the subject of intense research during the last two decades.⁴⁻⁶ Today silver^{2,7} as well as other transition metal (catalytic) nanomaterials receive particular attention and are among the most active fields in nanoscience.^{5,8-10}

The main challenge with metal nanoparticles is that they tend to coalesce and aggregate.^{1,5} As a consequence, the catalytically active surface area reduces, and the particles may precipitate and lose their catalytic activity. Therefore, metal nanoparticles always require a suitable stabilization

to sustain their colloidal stability over long periods.^{11,12} For that purpose, the metal precursors are commonly reduced in the presence of soluble or colloidal stabilizing/capping agents.^{4,8,11} However, the metal surface must still be accessible for the reactants in catalysis, i.e., the surface must not be irreversibly and entirely covered by the stabilizer.⁵ For that purpose, numerous different approaches have been demonstrated, yielding more and more sophisticated systems, e.g., based on polymers,¹³⁻¹⁵ dendrimers,¹⁶⁻¹⁸ microgels¹⁹⁻²¹ or more complex colloidal systems.^{22,23}

Furthermore, if so-called responsive polymers are applied, the support provides an environment with additional functionality. Responsive polymers are polymers that are sensitive to stimuli such as *pH*,^{24,25} light,^{19,26} concentration of cosolutes,²⁷ or temperature.^{28,29} Hence, the catalytic activity of nanoparticles can be modulated externally.

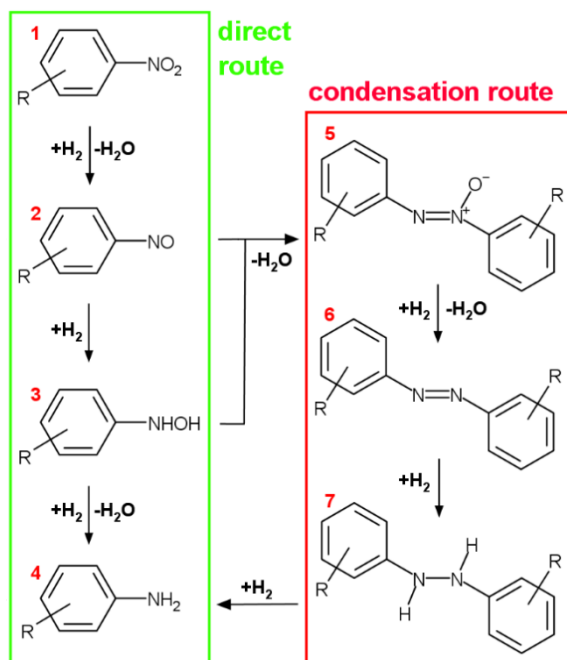


Figure 1. Reaction scheme for the reduction of nitroarenes. Direct route (green) and condensation route (red).

Hence, such systems are termed active carriers or nanoreactors.⁵

Recently, systems comprising the thermoresponsive polymer poly-*N*-isopropylacrylamide (PNIPAM) are under intense research due to their potential use in biomedical applications^{30–32} and catalysis.^{5,33} PNIPAM exhibits a so-called lower critical solution temperature (LCST). It is hydrophilic at low temperatures and becomes hydrophobic above its LCST of $T = 32\text{ }^\circ\text{C}$.^{34,35} As a consequence, hydrogel networks of PNIPAM undergo a volume transition upon heating where they expel water, and the hydrogel collapses. This functionality enables the external control of their catalytic activity in a non-Arrhenius way through simple temperature adjustment.^{20,28,36} In first-order kinetic analyses, the non-Arrhenius behavior of the reaction rate could be fully traced back to a complex temperature dependence of the partitioning coefficient (i.e. the ratio of the reactant concentration inside/outside the hydrogel network) and permeability behavior of the hydrogel across the volume transition, explicitly discussed for the first time from a theoretical perspective.^{5,37–41} To assess the catalytic activity of different catalysts, so-called model reactions are applied, which offer the possibility for reproducible and easy-to-handle measurement of reaction rates of different catalysts or at different reaction conditions.^{5,6}

The reduction of 4-nitrophenol (NO_2) to 4-aminophenol (NH_2) with borohydride has been first suggested as a model reaction by Pal et al. and Esumi et al.^{42,43} Since then, it has gained tremendous interest and is nowadays the most widely used benchmark reaction to evaluate the catalytic activity of all varieties of metal-based nanocomposites.^{5,12} The reduction was shown to take place only in the presence of a metal catalyst and the reaction rate to be

proportional to the metal surface area present in the reaction mixture, showing that the reaction takes place on the surface of the catalyst metal.^{44,45}

The general reaction scheme for the reduction of nitroarenes, shown in Figure 1, was first established by Haber in 1898.⁴⁶ Two reaction routes were identified.⁴⁷ In the *direct route*, nitroarenes (1) yield the respective arylamine (4) in three reaction steps via nitroso (2) and hydroxylamine (3) intermediates. In the *condensation route*, the latter two intermediates undergo a condensation reaction in solution, yielding an azoxy intermediate (5), which is subsequently reduced to the respective arylamine via azo (6) and hydrazo (7) intermediates. If the intermediates (2) and (3) are not adsorbed strong enough to the catalyst surface and desorb during the reaction, the *condensation route* mechanism could occur as an undesired parallel reaction to the desired *direct route*. Therefore, utmost care is necessary during the kinetic evaluation to ensure that the reaction satisfies the prerequisites of model reactions. If the reaction kinetics are monitored by UV-Vis spectroscopy, the presence of isobestic points (where all spectra intersect) is commonly accepted as a sign that only the reactant and product are present at varying concentrations in solution. Hence, the prerequisites for model reactions are regarded as fulfilled.

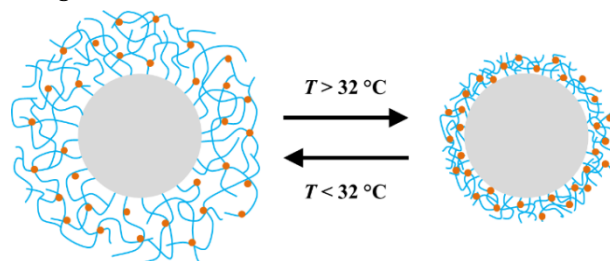


Figure 2. Core-shell nanoreactors, comprising of a PS core (grey), a thermoresponsive PNIPAM shell (blue), and silver nanoparticles, immobilized in the shell (orange). Upon heating above (cooling below) $T = 32\text{ }^\circ\text{C}$, the network changes its volume and shrinks (swells).

In this work, PS-PNIPAM core-shell nanoreactors, comprising of a polystyrene (PS) core and a PNIPAM shell, crosslinked with *N,N'*-methylenebisacrylamide (Bis), are used as support for silver nanoparticles (Ag@PS-PNIPAM) as shown in Figure 2.

We present a detailed spectral analysis of the reduction of NO_2 with borohydride to verify the absence of intermediates in solution, exclude that the reaction follows (partly) the condensation route, and to obtain the time dependency of the product (NH_2) concentration. Therefore, the UV-Vis spectra recorded during the reduction are deconvoluted with the Levenberg-Marquardt algorithm (LMA).^{48–50} The latter uses the entire UV-Vis spectra in a range from 240 to 500 nm to obtain the precise concentration-time dependencies of all species present in the reaction mixture. Furthermore, we demonstrate the potential of the LMA as a general assessment tool for model reactions.

For the reaction catalyzed by gold nanoparticles, a model has been developed which could successfully describe

the full kinetics of the NO_2 reduction on different metals.⁵¹⁻⁵³ Here, we investigate the reaction on silver to expand the existing picture of the kinetics. We present a kinetic model, based on the results of the LMA, and investigate the kinetics at a constant temperature. Additionally, the effect of the thermoresponsive PNIPAM hydrogel on the kinetics is investigated with measurements at different temperatures to evaluate the influence of the partitioning coefficients of the reactants and products on the kinetics.

Experimental

Materials

Styrene ($\geq 99\%$; stabilized with 250 ppm dibutylated hydroxytoluene; BHT), *N*-isopropylacrylamide (NIPAM; $\geq 97\%$), *N,N'*-methylenebisacrylamide ($\geq 99\%$), sodium dodecylsulfate (SDS; $\geq 99\%$), 4-nitrophenol ($\geq 99\%$), and BHT inhibitor remover, all obtained from Sigma-Aldrich; potassium peroxydisulfate (KPS; $\geq 99\%$) and silver nitrate ($\geq 99.5\%$), both from Fluka; 4-aminophenol ($\geq 99\%$; Merck), sodium borohydride ($\geq 99\%$; Acros), buffer (boric acid-based; $pH = 10$; Carl Roth), and 4,4'-dihydroxy azobenzene (*HNNH*; $\geq 98\%$; TCI) were used without further purification. Styrene was run over a column packed with inhibitor remover and stored at $T = 5^\circ C$ prior to use. Millipore water ($R = 18.2 M\Omega$) was used throughout all preparations and experiments. Ultrafiltration was performed with nitrocellulose membranes (Millipore) with 50 and 100 nm pore sizes, respectively.

Nitrosophenol (*NO*; water content $\sim 40\%$; TCI) was purified according to a modified literature procedure.⁵⁴ After drying in vacuum at $T = 40^\circ C$ overnight, *NO* was dissolved in anhydrous diethyl ether, the insoluble residue was filtered off and remaining water was removed over a molecular sieve (4 Å mesh size) overnight. After removing the ether, the crude product was redissolved in dry ether (20 g L⁻¹), and a green solution was obtained. Upon adding the 2.5-fold volume of dry hexane to the solution, orange crystal needles precipitated, were filtered off, dried in vacuum, and stored at $T = 4^\circ C$.

Synthesis

Synthesis of the Ag@PS-PNIPAM nanoreactors was carried out as described elsewhere.^{55,56}

Polystyrene core particles were prepared by emulsion polymerization. A mixture of SDS (0.45 g), styrene (30 g), and NIPAM (1.63 g) in 250 mL H₂O was heated to $T = 80^\circ C$. KPS (0.3 g; dissolved in 20 mL H₂O) was added to initiate the polymerization and the mixture was stirred at 250 rounds per minute (rpm) for 8 hours. After cooling down and filtering over glass wool, the suspension was purified by ultrafiltration until the permeate reached a conductivity of $\sigma \leq 30 \mu S cm^{-1}$. A particle suspension with a mass concentration of $c_m = 67.6 g L^{-1}$ was obtained.

PS-PNIPAM core-shell particles were prepared by seeded emulsion polymerization. A mixture of the precursor PS core particle suspension (28.3 ml), NIPAM (2.1 g), Bis (0.072 g), and additional 92 ml H₂O was heated to $T = 80^\circ C$. KPS (0.3 g; dissolved in 20 mL H₂O) was added, and the mixture was stirred at 250 rpm and for 4.5 hours.

After cooling down and filtering over glass wool, the suspension was purified by ultrafiltration until the permeate reached a conductivity of $\sigma \leq 2 \mu S cm^{-1}$. A particle suspension with a mass concentration of $c_m = 4.2 g L^{-1}$ was obtained.

Ag@PS-PNIPAM nanoreactors were prepared by in-situ reduction of AgNO₃ by NaBH₄. Silver nitrate (0.045 g in 30 mL H₂O) was added dropwise to an aqueous dispersion of 0.3 g PS-PNIPAM core-shell particles in 260 mL H₂O over 30 minutes. After stirring for another 2 hours, the mixture was degassed for 30 minutes and cooled with an ice bath. NaBH₄ (0.06 g in 20 mL H₂O) was added dropwise over 30 minutes, and the suspension was stirred for another 30 minutes before filtering over glass wool and subsequent ultrafiltration until the permeate reached a conductivity of $\sigma \leq 1 \mu S cm^{-1}$. A stock catalyst suspension with a mass concentration of $c_m = 0.194 g L^{-1}$ was obtained.

Instrumentation

Cryogenic transmission electron microscopy

Cryogenic transmission electron microscopy (cryo-TEM) measurements were conducted on a JEM 2100 microscope (JEOL) equipped with a LaB₆ cathode and a Gatan 914 holder (Gatan) for cryogenic measurements. Samples were prepared on lacey carbon grids (200 mesh Cu; Science Services), which were pre-treated by glow discharge for about one minute. 4 μL of the sample was applied on a grid and vitrified in liquid ethane with a Vitrobot™ (FEI). The blotting conditions were *blot force* = 0 N, *blot time* = 1 s, *humidity* = 100%, *wait-* and *drain time* = 0 s and $T = 5^\circ C$. The microscope was operated at an acceleration voltage of 200 kV, and images were recorded with a Tem Cam F416 camera (TVIPS) by aid of the SerialEM software⁵⁷ and further processed with ImageJ v.1.49 (Wayne Rasband, National Institute of Health, USA).

Dynamic light scattering

Dynamic light scattering (DLS) measurements were carried out on a Zetasizer Nano ZS ZEN 3500 (Malvern Instruments), equipped with a He-Ne Laser ($\lambda = 633 nm$). Measurements were performed in PS cuvettes (VWR) at a mass concentration of $c_m = 50 mg L^{-1}$, using Millipore water for dilution and analyzed with the proprietary Zetasizer Software v.7.11 (Malvern Instruments). For a typical measurement, ten runs of 30 seconds duration were measured at a scattering angle of 173° and averaged. For the thermoresponsive core-shell microgels, temperature-dependent measurements with a range from $T = 10$ to $50^\circ C$ and a step size of $2.5^\circ C$ were conducted.

Thermogravimetric analysis

Thermogravimetric analysis (TGA) was performed on a STA 409PC Luxx (Netsch). For a typical measurement, about 15 mg of previously freeze-dried sample was filled into a crucible and heated to $T = 800^\circ C$. The measurements were conducted with a heating rate of $10 K min^{-1}$ under argon flow (30 mL min⁻¹), and the temperature was held constant at $T = 800^\circ C$ for 1 hour.

UV-Vis

UV-Vis spectroscopy was performed in QS-110 cuvettes (Hellma), using an Agilent 8453 spectrophotometer (Agilent), equipped with a K6s-NR thermostat ($\Delta T \leq 0.1$ °C; Huber). Baseline correction was recorded against pure water for all measurements.

Kinetic measurements

For the kinetic measurements, all solutions were properly degassed before use and held under N_2 . $NaBH_4$ was dissolved in previously degassed water under N_2 prior to each measurement. All solutions were pipetted into a thermostatted cuvette and held under N_2 until the catalyst was added last. Like that, oxygen could be excluded to that extent that no induction time was observed (i.e. too short to be resolved until the measurement was initiated). Subsequently, the cuvette was sealed, turned once for mixing, and immediately subjected to measurement. For the kinetic measurements, spectra from $\lambda = 240$ to 500 nm were recorded every 5 seconds. A detailed description of the measurement protocol is provided in the Supporting Information.

Results and discussion

Characterization

The Ag@PS-PNIPAM nanoreactors were characterized by cryo-TEM, DLS and TGA. Figure 3 shows a typical cryo-TEM image of the Ag@PS-PNIPAM core-shell nanoreactors. The image shows the PS core as large dark spheres, surrounded by the silver nanoparticles (small black dots), which are predominantly located close to the surface of the PS cores. The PNIPAM shell (with a diameter of around 200 nm in Figure 3) is hardly visible around the PS cores because the hydrogel swollen with water gives only a very weak contrast in the images, which is difficult to be distin-

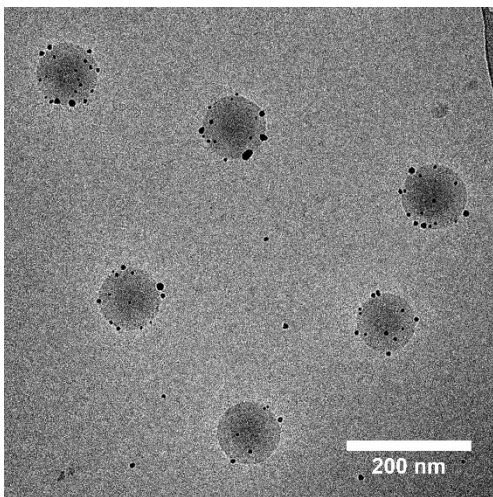


Figure 3. Cryo-TEM image of the Ag@PS-PNIPAM core-shell nanoreactors vitrified at $T = 5$ °C. The large spheres are the PS core particles, surrounded by silver nanoparticles visible as small black dots. The PNIPAM shell is hardly visible as halo around the PS core particles.

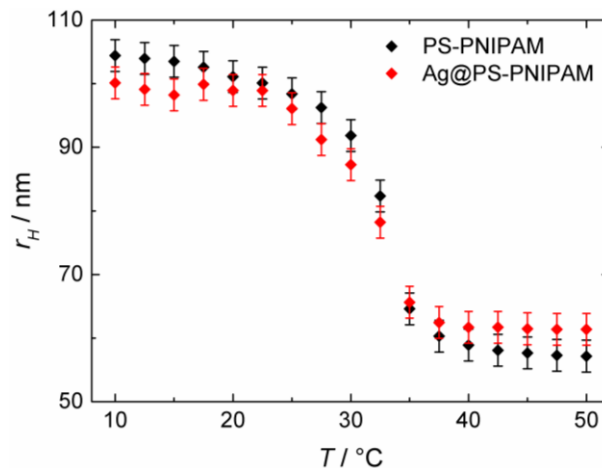


Figure 4. Hydrodynamic radii of the core-shell nanoreactors before and after the reduction of silver nanoparticles.

guished by our cryo-TEM instrument without energy filter. However, the existence of a thermoresponsive shell is undoubted, as disclosed by the measurements of the hydrodynamic radii against temperature in Figure 4.

The size of the silver nanoparticles was determined via cryo-TEM images. Therefore about 400 particles were measured to obtain the representative average nanoparticle diameter of $d_{Ag} = 5.6 \pm 2.4$ nm. The obtained size distribution of the silver nanoparticles is provided in the Supporting Information.

After each synthesis step, the particle size was determined via DLS. For the core particles, a hydrodynamic radius of $r_H = 52.6$ nm was obtained. For the core-shell structure the size was determined between $T = 10$ and 50 °C, both, before and after the preparation of the silver nanoparticles. The results in Figure 4 show the expected collapse of the PNIPAM network upon heating to be in accordance with previous results.^{20,36,58,59} Between $T = 25$ and 35 °C the particle radius shrinks to about 50% of its value at low temperatures. The steepest shrinkage is observed around the lower critical solution temperature (LCST) of $T = 32$ °C for PNIPAM, where the polymer changes from hydrophilic to hydrophobic, expels water and collapses.³⁵ The hydrodynamic radius remains essentially the same upon silver reduction; the differences are within the experimental error.

The silver mass fraction of the readily prepared Ag@PS-PNIPAM nanoreactors was determined via TGA. The weight loss of the nanoreactors before and after the synthesis of silver nanoparticles was determined, and the residual mass of the PS-PNIPAM nanoreactors was considered in the calculation, yielding a silver mass fraction of $f_{Ag} = 0.099$ for the dried catalyst.

Together with the average silver nanoparticle radius and the mass concentration of the Ag@PS-PNIPAM catalyst stock suspension, a silver surface area per unit volume of $S = 2.0$ m² L⁻¹ was obtained. The details of the calculations are provided in the Supporting Information.

Spectral decomposition

Prior to the kinetic analysis, the spectra recorded during the reduction of NO_2 with borohydride are analyzed. Previous kinetic studies were always based on the concentration-time dependency of NO_2 derived from its optical absorption maximum at $\lambda = 400$ nm. However, with this approach, only the reactant concentration can be monitored. Here, the full spectra recorded during the reduction from $\lambda = 250$ to 500 nm, shown in Figure 5 (a), are deconvoluted with the Levenberg-Marquardt algorithm (detailed in the Supporting Information) to obtain the product concentration as well and additionally verify the absence of intermediates in solution, which is a condition for model reactions.

Prerequisites for the decomposition are reference spectra of all species to be detected. Since the (wavelength-dependent) extinction coefficient curve of each species in solution represents a unique fingerprint, the experimental spectra can be regarded as a linear combination of n -dimensional vectors for each species. Here, n stands for the number of data points of the UV-Vis spectra.

The present analysis is based on the molar extinction spectra of the reactant NO_2 , the product NH_2 , one intermediate of the direct route NO , and one intermediate of the condensation route $HNNH$ as well as the spectrum of the catalyst (see Figures S 2 (a) and (b) in the Supporting Information).

With the reference spectra, the experimental spectra can be deconvoluted (exemplary shown in Figure 5 (b)). Only the reactant, the final product, and the catalyst yield significant contributions to the UV-Vis spectrum (the absorbance of the catalyst is subtracted for better visibility). Although a residual spectrum (green) was detected, the presence of NO and $HNNH$ in the solution can be excluded safely by the LMA. The residual spectrum in Figure 5 (b) as well as the residual spectra recorded during the entire course of reaction (see Figure S 2 (c) in the Supporting Information) exhibit an overall low intensity compared to the absorption of the original spectra.

The resulting concentration-time curves of the concentration of NO_2 , c_{NO_2} , NH_2 , c_{NH_2} , and their sum concentration (normalized to the initial concentration of NO_2 $c_{NO_2,0}$) in Figure 5 (c) show that the sum concentration of NO_2 and NH_2 is constant to $\Delta c < 1\%$ of the initial NO_2 concentration. This result shows that NO_2 is converted to NH_2 via the direct route while intermediates (NO and 4-hydroxylaminophenol) remain adsorbed, hence no reaction along the *condensation route* can occur. Additionally, the first derivatives of NO_2 and NH_2 in Figure 5 (c) coincide with high precision, emphasizing further that NO_2 is directly transferred to NH_2 without accumulation of intermediates.

The presence of isosbestic points in the UV-Vis spectra (where all spectra intersect in Figure 5 (a)) is commonly accepted as a sign that only two species of varying concentration (i.e., the reactant NO_2 and the product NH_2) are present in solution and that the reaction takes place solely along the desired *direct route*. However, in some cases,

isosbestic points are not clearly discernible.^{29,60-63} For such cases, the above spectral decomposition provides a tool to verify whether the reaction does or does not run solely along the *direct route*.

Additionally, the spectra of NO_2 and NO are very similar and both species show an absorption maximum at $\lambda = 400$ nm (see Figure S 2 (a)). Therefore, it is theoretically possible that the absorbance at this wavelength, which is commonly used to follow the NO_2 concentration for the kinetic evaluation according to

$$\frac{Abs(t) - Abs(t=\infty)}{Abs(t=0) - Abs(t=\infty)} = \frac{c_{NO_2}}{c_{NO_2,0}} \quad (1)$$

comprises contributions from NO as well.

Furthermore, the almost identical extinction curves of NO_2 and NO at both isosbestic points (at $\lambda = 280$ and 315 nm of the spectra in Figure 5 (a)) would result in isosbestic points, even if all three species NO_2 , NO , and NH_2 are present in solution at varying concentrations. Deriving the NO_2 concentration from the absorbance at $\lambda = 400$ nm would then result in a wrong concentration-time curve, although the presence of isosbestic points would give deceptive confidence of a model reaction with only two species present. However, the application of the LMA will avoid this pitfall during data evaluation and serves as an assessment tool for model reactions at the same time.

The LMA, enables a safe discrimination, even of species with very similar spectra like NO_2 and NO . Figure 5 (d) illustrates a case where NO_2 and NO are mixed ($c_{NO_2} = c_{NO} = 2.5 \times 10^{-5} \text{ mol L}^{-1}$). The LMA discriminates NO_2 and NO with the fitted concentrations $c_{NO_2} = 2.32 \times 10^{-5} \text{ mol L}^{-1}$ and $c_{NO} = 2.84 \times 10^{-5} \text{ mol L}^{-1}$, respectively. Assuming an error of $\Delta c \leq 5\%$ during solution preparation, the LMA yields the correct concentrations with an average error of $\Delta c \sim 5\%$. This can be considered as a good value for species with very similar spectra and would be lower for spectra with more pronounced differences.

Overall, the adaptability of the LMA, which only requires reference spectra of the species to be detected, makes it a versatile tool to test the applicability of a reaction as a model reaction. Here, the LMA is applicable to any reaction which can be measured with UV-Vis spectroscopy or even other measurement techniques, yielding spectra which are a simple sum of the separate spectra of different species in a reaction mixture.

For the present case, the curves of the concentration of NO_2 , obtained via spectral decomposition, and obtained from the absorption maximum of NO_2 at $\lambda = 400$ nm, according to equation (1), are virtually identical (see Figure S 3 in the Supporting Information). Therefore, the following kinetic analysis can be based on the latter.

The pivotal result of the LMA for the following kinetic analysis is that it evinces the direct conversion of NO_2 to NH_2 without the accumulation of intermediates. This is the basis for the kinetic model presented hereafter.

Kinetic model

The model for the analysis of the reduction catalyzed by

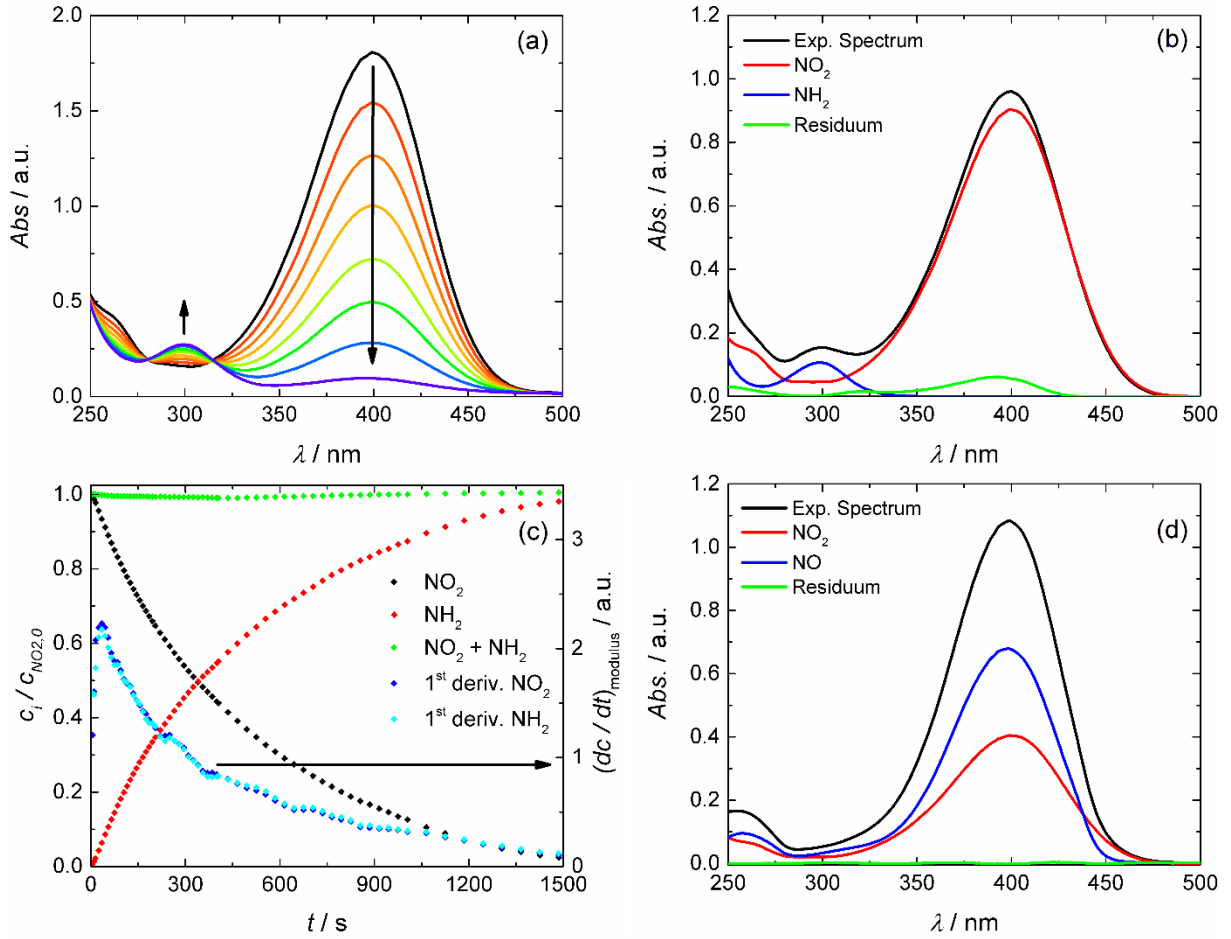


Figure 5. Absorption spectra (a) recorded during NO_2 reduction (arrows indicate the course of reaction), exemplary experimental absorption spectrum (b) recorded during the reduction of NO_2 with resulting deconvoluted spectra for NO_2 , NH_2 , and the residual spectrum, obtained concentration-time curves (c) for NO_2 , NH_2 , the sum concentration of both (normalized to $c_{NO_2,0} = 1 \times 10^{-4} \text{ mol L}^{-1}$), and modulus of the first derivatives for NO_2 and NH_2 , and exemplary spectrum of a mixture of NO_2 and NO (d) with resulting deconvoluted spectra for NO_2 , NO , and the residual spectrum.

Ag@PS-PNIPAM nanoreactors is based on the two-step model applied for the analysis of the reaction on gold and gold-palladium alloy catalysts by Gu et al.⁵¹⁻⁵³ Here, the reaction of NO_2 to 4-hydroxylaminophenol ($NHOH$) is regarded as the first reaction step with the rate constant k_a (the reaction step of NO to $NHOH$ is fast, therefore the reaction of NO_2 to NO and further to $NHOH$ is considered as one step)^{51,64} and the reaction of $NHOH$ to NH_2 is regarded as second reaction step with the rate constant k_b . Additionally, the adsorption of the reaction product NH_2 is considered in the present model.

The differential rate equations for the temporal evolution of the concentrations of NO_2 and $NHOH$ are then given as^{51,65}

$$-\frac{dc_{NO_2}}{dt} = \frac{k_a S (K_{ad,NO_2} c_{NO_2})^n K_{ad,BH_4} c_{BH_4}}{(1 + (K_{ad,NO_2} c_{NO_2})^n + K_{ad,NHOH} c_{NHOH} + K_{ad,BH_4} c_{BH_4} + K_{ad,NH_2} c_{NH_2})^2} \quad (2)$$

and

$$\frac{dc_{NHOH}}{dt} = -\frac{dc_{NO_2}}{dt} - \frac{dc_{NH_2}}{dt} = \frac{SK_{ad,BH_4} c_{BH_4} (k_a (K_{ad,NO_2} c_{NO_2})^n - k_b K_{ad,NHOH} c_{NHOH})}{(1 + (K_{ad,NO_2} c_{NO_2})^n + K_{ad,NHOH} c_{NHOH} + K_{ad,BH_4} c_{BH_4} + K_{ad,NH_2} c_{NH_2})^2} \quad (3)$$

where K_{ad,NO_2} , $K_{ad,NHOH}$, K_{ad,NH_2} and K_{ad,BH_4} are the adsorption constants of NO_2 , $NHOH$, NH_2 , and borohydride (supposedly; see chapter "Influence of temperature" for a detailed discussion), and c_{NHOH} and c_{BH_4} are the concentrations of $NHOH$ and borohydride, respectively. A brief derivation of equations (2) and (3) is provided in the Supporting Information. Here, the adsorption of NO_2 is modeled with a Langmuir-Freundlich adsorption isotherm with the unitless surface heterogeneity parameter n .^{65,66} Prerequisite for the applicability of equations (2) and (3) (as well as generally for all models based on Langmuir-Hinshelwood kinetics) is that the surface reaction rate is slow (i.e., the rate-determining step) compared to the diffusion of reactants to the catalyst surface, which was shown to be true for the NO_2 reduction.⁶⁷ A theoretical treatment of the reaction rate for (catalyzed) unimolecular reactions in

core-shell nanoreactors with multiple active catalyst particles, accounting for variable rates of reaction and diffusion, was presented by Piazza et al.³⁹ Despite treating the geometry of the catalyst used in this work, the theory cannot readily be connected to the present kinetic model of a two-step reaction accounting for the competitive adsorption of multiple species. However, it showed that for our specific geometry, the rate (in the reaction-controlled limit) must be linearly proportional to the catalyst metal surface area and the partitioning coefficient, justifying our ansatz (2) for the total rate and as well the separation of adsorption constants and partition ratios in eq. (14) later in the analysis.

The decomposition of the UV-Vis spectra recorded during the reduction of NO_2 showed that the decrease in the reactant (NO_2) concentration directly corresponds to the increase in the concentration of the final product NH_2 with high precision. No accumulation of the intermediates occurs and the reaction runs cleanly along the *direct route*, as desired for the kinetic evaluation. Hence, a stationary state for the concentration of the intermediate $NHOH$ is present from the very beginning of the reaction onwards and therefore

$$-\frac{dc_{NO_2}}{dt} = \frac{dc_{NH_2}}{dt}. \quad (4)$$

Thus, the concentration of NH_2 can be derived from the NO_2 concentration according to

$$c_{NH_2} = c_{NO_2,0} - c_{NO_2}. \quad (5)$$

With equation (2) and (3) it follows that

$$K_{ad',NHOH}c_{NHOH} = \frac{k_a}{k_b}(K_{ad',NO_2}c_{NO_2})^n, \quad (6)$$

$K_{ad',NHOH}c_{NHOH}$ can be substituted in equation (2), and the rate equation for the reactant is derived as

$$-\frac{dc_{NO_2}}{dt} = \frac{k_a S (K_{ad',NO_2}c_{NO_2})^n K_{ad',BH_4}c_{BH_4}}{\left(1 + \left(1 + \frac{k_a}{k_b}\right)(K_{ad',NO_2}c_{NO_2})^n + K_{ad',BH_4}c_{BH_4} + K_{ad',NH_2}c_{NH_2}\right)^2}. \quad (7)$$

Equation (7) was described previously for the stationary state of the reduction by gold nanoparticles (without the term for the adsorption of the product NH_2 in the denominator). However, as a stationary state was not present from the beginning of the reaction, it could not describe the entire kinetics.⁵¹ Here, it provides a full description of the kinetics of the reaction with the six fitting parameters k_a , k_b , K_{ad',NO_2} , K_{ad',NH_2} , K_{ad',BH_4} , and n . A closer look reveals that equation (7) is underdetermined. Substituting the fit parameters with

$$K_1 = k_a(K_{ad',NO_2})^n \quad (8)$$

and

$$K_2 = \left(1 + \frac{k_a}{k_b}\right)(K_{ad',NO_2})^n \quad (9)$$

reduces their number to five and equation (7) is obtained as

$$-\frac{dc_{NO_2}}{dt} = K_1 S \frac{(c_{NO_2})^n K_{ad',BH_4}c_{BH_4}}{\left(1 + K_2(c_{NO_2})^n + K_{ad',BH_4}c_{BH_4} + K_{ad',NH_2}c_{NH_2}\right)^2}. \quad (10)$$

The substitution of fit parameters shows that for the present model (describing a reaction where a stationary state is present from the beginning of the reaction), it is impossible to obtain the two reaction rate constants k_a and k_b separately. Without a stationary state from the beginning, it is indeed possible to obtain k_a and k_b separately as shown by Gu et al. with gold nanoparticles.⁵¹ However, a reduced reaction rate constant k_{red} can be obtained from the two substituted parameters K_1 and K_2 as

$$\frac{K_1}{K_2} = k_{red} = \frac{k_a k_b}{k_a + k_b}. \quad (11)$$

This is reasonable, considering that NO_2 is directly reduced to NH_2 without accumulation of intermediates in solution. Both reaction steps are coupled, and the ratio K_1/K_2 can be regarded as the overall reaction rate, similar to the classic expression for catalyzed unimolecular reactions^{5,40,41}

$$k_{tot}^{-1} = k_D^{-1} + k_R^{-1}, \quad (12)$$

which also describes two coupled consecutive steps (with the diffusion rate k_D and the reaction rate k_R) by a total reaction rate k_{tot} .

Two limiting cases can be distinguished:

If a) $k_a \gg k_b$, $K_1/K_2 \rightarrow k_b$ follows, the intermediates will accumulate on the catalyst surface, and slow down the overall reaction to k_b . The spectral decomposition revealed that the sum concentration of NO_2 and NH_2 remains constant throughout the whole reaction. This observation means that in this case, the adsorption of the intermediate must be sufficiently high to suppress its desorption.

If b) $k_a \ll k_b$, $K_1/K_2 \rightarrow k_a$ follows, and the intermediates are immediately reduced to products without accumulating on the catalyst surface. Furthermore, equation (10) reduces to the classic one-step Langmuir-Hinshelwood kinetics^{68,69} (with Freundlich adsorption isotherm if $n < 1$)⁶⁵ as K_2 reduces to $K_2 = (K_{ad',NO_2})^n$. This shows that the present two-step Langmuir-Hinshelwood model is mathematically indistinguishable from the classical one-step model and only the interpretation of the obtained fit parameters K_1 and K_2 differs. As k_b disappears if $k_a \ll k_b$, the initial number of fit parameters is reduced to five, equation (7) is not underdetermined, and K_{ad',NO_2} can be derived as well.

Kinetic analysis at a constant temperature

For the kinetic analysis at $T = 20$ °C, measurements at three NO_2 and three borohydride concentrations were conducted, yielding a 3×3 matrix. All measurements were conducted at a ratio of borohydride to NO_2 concentration of $c_{BH_4}/c_{NO_2} \geq 50$. Therefore, the borohydride concentration can be regarded as constant throughout every single experiment. All experiments were conducted three times and averaged. The catalyst surface area per unit volume was $S = 0.0625$ m² L⁻¹. Consistent with previous results on gold, platinum, ruthenium and silver catalysts, the reaction

rate is increasing with increasing borohydride concentration, and decreasing with increasing NO_2 concentration.^{17,18,65} Even though the borohydride concentration is much higher than the NO_2 concentration, a change in the (initial) borohydride concentration influ-

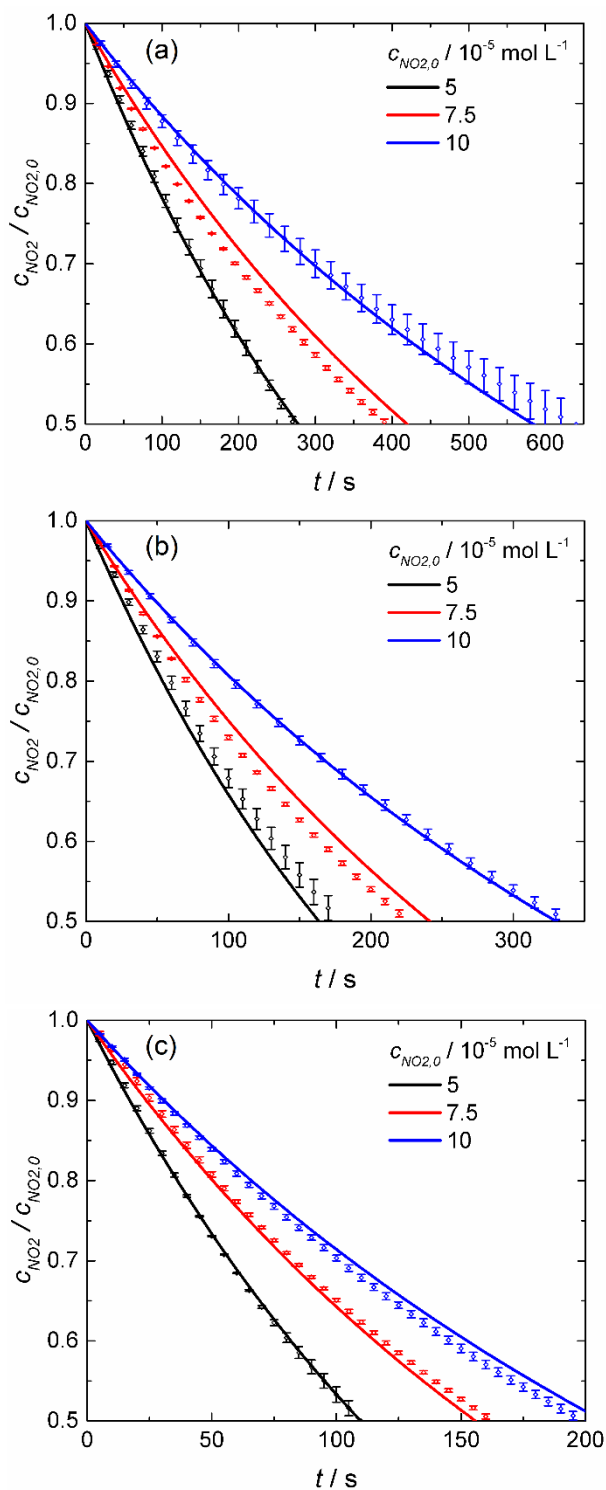


Figure 6. Time dependencies of the experimental NO_2 concentration (symbols) and fit results (lines) for the reduction at $c_{BH_4} = 5 \times 10^{-3}$ (a), 1×10^{-2} (b), and 2×10^{-2} mol L^{-1} (c).

ences the surface coverage of both reactants and, hence, has an influence of the observed reaction rate. The subsequent fit with only one set of fit parameters for all nine measurement conditions demonstrates that the reason for an influence of the borohydride concentration on the reaction rate originates from the different adsorption constants of borohydride and NO_2 .

All data were fitted globally up to a conversion limit of 50%. A detailed description and the code for the fit algorithm are provided in the Supporting Information. The fit results in Figure 6 show that the model fits the data with high precision up to the conversion limit of 50%.

Fits with a model, disregarding the adsorption of NH_2 showed a strong deviation between experimental data and fit where the analysis of the deviation points to the adsorption of NH_2 . Hence, the latter is included in the model presented here. The respective fits without NH_2 and a detailed discussion of the deviation are provided in the Supporting Information.

The obtained fit parameters for both limiting cases, a faster first ($k_a \gg k_b$) and a faster second reaction step ($k_a \ll k_b$) are $n = 0.788$, $K_{ad',BH_4} = 35.8$ L mol $^{-1}$, $K_{ad',NH_2} = 1.81 \times 10^4$ L mol $^{-1}$, $K_1 = 0.110$ L n mol $^{1-n}$ m $^{-2}$ s $^{-1}$, $K_2 = 2.06 \times 10^3$ L n mol $^{-n}$ and $k_{red} = 5.32 \times 10^{-5}$ mol m $^{-2}$ s $^{-1}$.

The fit parameters n and K_{ad',BH_4} are of the same order of magnitude as the values obtained previously on gold ($n = 0.5$ and $K_{ad,BH_4} = 50 \pm 4$ L mol $^{-1}$).⁵¹ The higher value of n , obtained in the present work, points to a more uniform surface of the silver nanoparticles compared to the gold nanoparticles in the aforementioned work (recall that the parameter n accounts for the distribution of adsorption energies due to the heterogeneity of the surface where $n = 1$ represents a completely uniform surface).^{66,70} Considering that a larger particle size automatically means less curvature and accordingly fewer edges and defects, this result is in accordance with the larger size of the silver nanoparticles in the present work ($d_{Ag} = 5.6 \pm 2.4$ nm compared to $d_{Au} = 4.4 \pm 0.8$ nm).⁶⁵ The reduced reaction rate is slightly lower than the reaction rate of the slower reaction step in the kinetic model applied on gold ($k_b = 5.6 \times 10^{-5}$ mol m $^{-2}$ s $^{-1}$).⁵¹ Together with the slightly lower value of K_{ad,BH_4} , this fits with our general experience of a slower reduction of NO_2 on silver compared to gold.^{71,72}

If $k_a \ll k_b$, the (supposed) adsorption constant of NO_2 can be derived as $K_{ad',NO_2} = 1.61 \times 10^4$ L mol $^{-1}$ and the reduced reaction rate constant k_{red} represents the rate constant k_a of the first reaction step. The latter is more than one order of magnitude lower than the value obtained previously on gold ($k_a = 9.4 \times 10^{-4} \pm 2.6 \times 10^{-4}$ mol m $^{-2}$ s $^{-1}$)⁵¹ while the adsorption constant of NO_2 , obtained on silver, would be over four times higher than on gold ($K_{ad,NO_2} = 3.70 \times 10^3$ L mol $^{-1}$).⁵¹

Influence of temperature

Measurements were conducted in intervals of $\Delta T = 5$ °C between $T = 10$ and 50 °C, and at concentrations of $c_{NO_2} = 1 \times 10^{-4}$ and $c_{BH_4} = 1 \times 10^{-2}$ mol L^{-1} to investigate the

influence of temperature on the reaction. All experiments were conducted three times and averaged. Here, the data were fitted individually for each temperature up to a conversion limit of 50%.

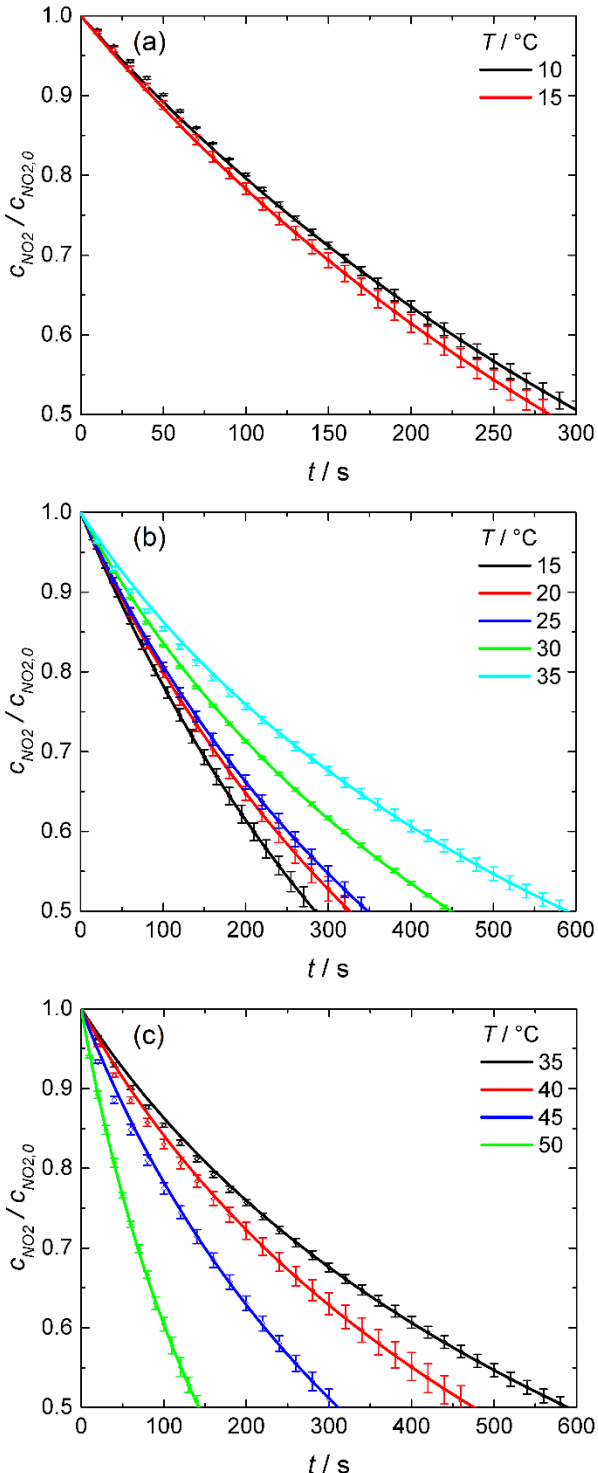


Figure 7. Time dependencies of the experimental NO_2 concentration (symbols) and fit results (lines) for the reduction at $T = 10$ to 50 °C and $S = 0.0625$ $m^2 L^{-1}$. The data were fitted up to 50% conversion.

As n is a measure for the heterogeneity of the catalyst surface, the parameter is expected to be approximately constant at moderate temperatures. In the previous section, nine experimental curves were simultaneously (globally) fitted, which leaves little freedom to the (genetic) fit algorithm in terms of letting the fit parameters work against each other (i.e. compensating the change in one parameter by the change in another one). As a good fit quality was obtained, these fit parameters are regarded as reliable reference values for the fits at other temperatures where only one curve is fitted at once. Therefore, the parameter n is fixed to the value obtained in the global fit at $T = 20$ °C and the number of fit parameters is reduced by one. This will help to obtain more reliable results in the Individual fits.

The experimental NO_2 concentrations in Figure 7 show that with increasing temperature, the reaction rate increases first between $T = 10$ and 15 °C, followed by a decrease up to $T = 35$ °C before it increases again. The fit results show that the model fits the data satisfactorily for all temperatures. Overall, the temperature-dependent measurements are slightly better fitted than the data obtained at $T = 20$ °C, shown in the previous section, because only one experimental concentration-time curve is fitted at once (compared to nine curves fitted globally at $T = 20$ °C).

The results for the obtained fit parameters K_1 , K_2 , n , K_{ad',BH_4} and K_{ad',NH_2} , and for k_{red} , shown in Figure 8 (and summarized in Table 1), show that the obtained fit parameters (at $T = 20$ °C) are in good accordance with the parameters obtained in the previous section. This shows that despite a different number of experimental curves is fitted simultaneously, reliable fit results are obtained by the individual fits as well.

A separate interpretation of the temperature dependencies of the fit parameters K_1 and K_2 is not possible as they comprise three and four (temperature-dependent) variables, respectively. However, both variables exhibit a specific behavior around the LCST of PNIPAM (minimum in K_1 ; plateau in K_2).

For k_{red} , a non-Arrhenius dependency is obtained, which was found repeatedly for the reaction rate of PNIPAM-based thermoresponsive catalysts.^{20,36,58,59,73} The reduced reaction rate increases first at low temperatures, decreases then, and reaches a minimum around the LCST before it increases again. The lowest value of k_{red} is found at $T = 35$ °C, in accordance with the slowest concentration decay in Figure 7.

The red line in Figure 8 (b) shows a linear fit to k_{red} between $T = 40$ and 50 °C to derive the (Arrhenius) activation energy. Obviously, the linearity of k_{red} in this temperature regime is not ideal and neither is a fit to only three data points. However, it is the only regime where the effects of the PNIPAM hydrogel collapse on the reaction rate are expected to be minor (according to the hydrodynamic radius of the nanoreactors in Figure 4), where an approximate linearity in the Arrhenius plot of k_{red} would be expected, and is observed. The resulting value for the activa-

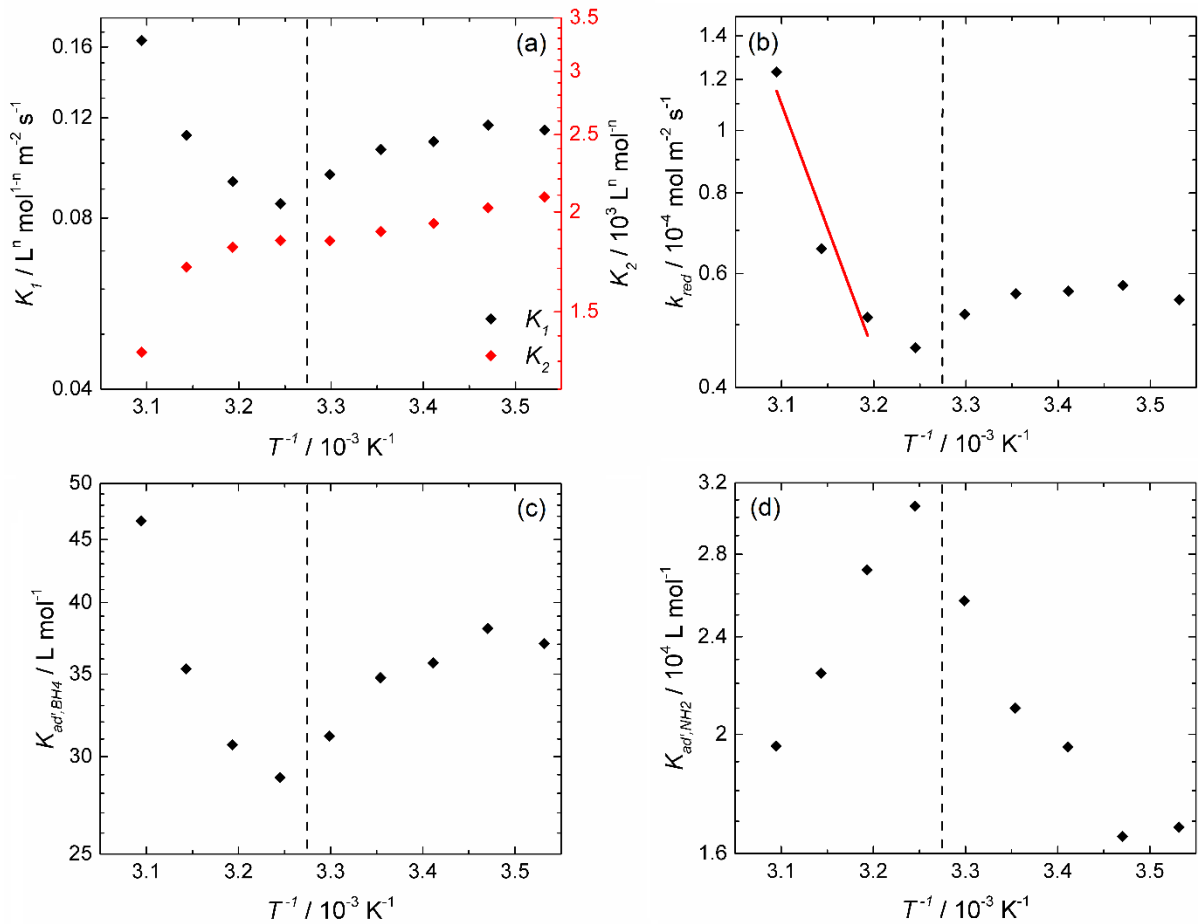


Figure 8. Arrhenius plots of the obtained fit parameters K_1 and K_2 (a), $k_{red} = K_1/K_2$ (b), and Van't Hoff plots of K_{ad',BH_4} (c), and K_{ad',NH_2} (d). The thin-dashed vertical lines indicate the LCST of $T = 32$ °C. The red line in (b) is a linear fit to k_{red} between $T = 40$ and 50 °C.

Table 1. Fit parameters obtained for the global fit at $T = 20$ °C and for the individual fits between $T = 10$ and 50 °C.

Fit type	$T / ^\circ\text{C}$	$K_1 / 10^{-3} \text{ L}^n \text{ mol}^{1-n} \text{ m}^{-2} \text{ s}^{-1}$	$K_2 / \text{L}^n \text{ mol}^{-n}$	$k_{red} / \text{mol m}^{-2} \text{ s}^{-1}$	$K_{ad',BH_4} / \text{L mol}^{-1}$	$K_{ad',NH_2} / \text{L mol}^{-1}$	n
global	20	0.110	2.06×10^3	5.32×10^{-5}	35.8	1.81×10^4	0.788
	10	0.114	2.09×10^3	5.47×10^{-5}	37.1	1.68×10^4	0.788
	15	0.117	2.02×10^3	5.76×10^{-5}	38.1	1.65×10^4	0.788
	20	0.109	1.94×10^3	5.64×10^{-5}	35.7	1.95×10^4	0.788
individual	25	0.106	1.89×10^3	5.59×10^{-5}	34.8	2.10×10^4	0.788
	30	0.096	1.84×10^3	5.19×10^{-5}	31.2	2.57×10^4	0.788
	35	0.085	1.84×10^3	4.61×10^{-5}	28.8	3.06×10^4	0.788
	40	0.093	1.81×10^3	5.14×10^{-5}	30.7	2.72×10^4	0.788
	45	0.112	1.71×10^3	6.56×10^{-5}	35.3	2.24×10^4	0.788
	50	0.164	1.33×10^3	1.23×10^{-4}	46.6	1.96×10^4	0.788

tion energy is with $E_a = 31.8 \text{ kJ mol}^{-1}$ close to the value which was reported for the first reaction step (k_a) on gold ($E_a = 36.1 \text{ kJ mol}^{-1}$).⁵¹

It may be seen as critical to derive an activation energy from a reduced reaction rate constant, comprising the rate

constants of two reaction steps according to equation (11). However, if one of the rate constants is much larger than the other, k_{red} is approaching the rate constant of the slower reaction step (v.s.: discussion of limiting cases) and the derived value represents the respective activation energy. Hence, the similarity of the obtained value to the

activation energy of the first reaction step on gold could mean that in the present case, the first reaction step is the slower step, i.e. $k_a \ll k_b$.

The Van't Hoff plots of K_{ad',BH_4} and K_{ad',NH_2} supposedly show the adsorption constants of borohydride K_{ad,BH_4} and NH_2 K_{ad,NH_2} alone. For the latter, though, a linear dependency would be expected in Figure 8 (c) and (d) according to the linearized Van't Hoff equation⁷⁴

$$\ln(K_{ad,i}) = \frac{1}{T} \left(-\frac{\Delta H_i}{R} \right) + \left(\frac{\Delta S_i}{R} \right), \quad (13)$$

where ΔH_i and ΔS_i are the enthalpy and the entropy of adsorption, respectively.

However, the kinetic model applies the bulk concentrations for borohydride, NO_2 , and NH_2 for a reaction that takes place at the surface of silver nanoparticles, immobilized inside the PNIPAM hydrogel. It is known that the actual concentration of solutes inside hydrogel networks can differ from their bulk concentration.^{41,75-77} The ratio of the concentration inside a hydrogel and in the surrounding bulk solution can be described by the partitioning coefficient according to^{5,37,75}

$$K_{part,i} = \frac{c_i^g}{c_i}, \quad (14)$$

where c_i^g and c_i are the concentrations of solute i inside and outside the hydrogel, respectively. Accordingly, the true concentration inside the hydrogel can be expressed by the product of the bulk concentration and the partitioning coefficient $K_{part,i}$. As the latter is not explicitly included in the present model, the derived constants $K_{ad',i}$ are expected to contain both, the adsorption constant $K_{ad,i}$ as well as the partitioning coefficient $K_{part,i}$ according to⁴⁰

$$K_{ad',i} = K_{ad,i} K_{part,i}. \quad (15)$$

This is then, of course, valid for all the supposed adsorption constants $K_{ad',NHOH}$, K_{ad',BH_4} , K_{ad',NH_2} , and K_{ad',NO_2} .

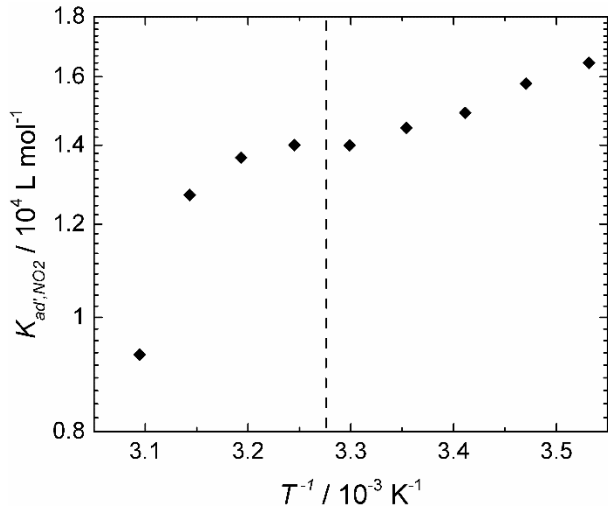


Figure 9. Van't Hoff plot of K_{ad',NO_2} , derived under the assumption $k_a \ll k_b$. The thin-dashed vertical lines indicate the LCST of $T = 32$ °C.

The latter can only be derived when $k_a \ll k_b$ is assumed. Figure 9 shows that the as-derived values of K_{ad',NO_2} are of the same order of magnitude as the values of K_{ad',NH_2} in Figure 8 (d). As the molecules NO_2 and NH_2 exhibit a similar structure, both their adsorption constant, as well as their partitioning coefficient, are not unlikely to be similar. Hence, similar values of the product of the latter (i.e., of K_{ad',NO_2} and K_{ad',NH_2}) may be another indication that the first reaction step is indeed the slower step.

For a further analysis of the data in Figures 8 (c) and (d) and Figure 9, the values of the adsorption constants and the partitioning coefficients, contained in $K_{ad',i}$ according to equation (15), need to be separated into the respective adsorption constants $K_{ad,i}$ and the partitioning coefficients $K_{part,i}$. Unfortunately, to our best knowledge, no data for the partitioning coefficients in PNIPAM, or the adsorption constants on silver, exist for borohydride, NH_2 , and NO_2 . Hence, Figures 8 (c) and (d), and Figure 9 can only qualitatively be analyzed hereafter.

To circumvent the lack of experimental values for the present system, the adsorption constants K_{ad,BH_4} and K_{ad,NO_2} , previously obtained on gold, are adopted.⁵¹ With these values, the partitioning coefficients can be derived according to equation (15) (i.e. $K_{part,i} = K_{ad',i}/K_{ad,i}$). The adsorption constants of borohydride and NO_2 were previously reported between $T = 10$ and 30 °C while the data in Figures 8 (c) and (d), and Figure 9 range up to $T = 50$ °C. Hence, the reported adsorption enthalpies and entropies of borohydride and NO_2 ($\Delta H_{BH_4} = 37 \text{ kJ mol}^{-1}$, $\Delta S_{BH_4} = 158 \text{ J mol}^{-1} \text{ K}^{-1}$, $\Delta H_{NO_2} = 24 \text{ kJ mol}^{-1}$, $\Delta S_{NO_2} = 150 \text{ J mol}^{-1} \text{ K}^{-1}$) are used to derive their adsorption constants K_{ad,BH_4} and K_{ad,NO_2} with (the Van't Hoff) equation (13) for the entire required temperature range.⁵¹ Transferring the adsorption constants from gold to silver may not be an ideal solution.

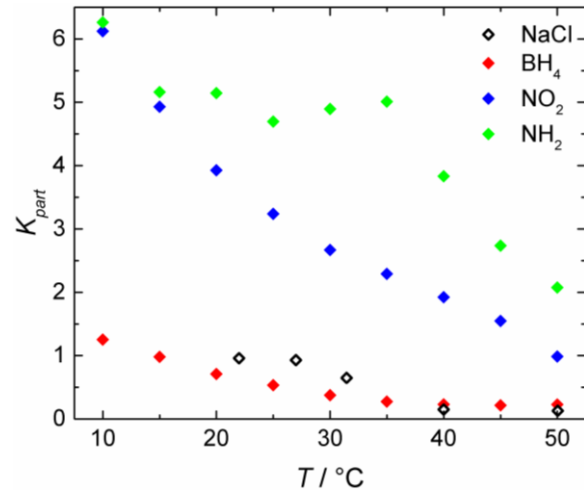


Figure 10. Derived partitioning coefficients for borohydride, NO_2 and NH_2 (filled symbols) and values for the partitioning coefficient of NaCl in a PNIPAM hydrogel, measured by Kawasaki et al. (open symbols).⁷⁸

However, the respective values for silver can be expected to be of the same order of magnitude as for gold and, hence, provide a basis for at least a qualitative interpretation.

The present kinetic model includes the adsorption of NH_2 for the first time, thus, no values for its adsorption constant exist yet. Here, the adsorption constant of NO_2 is adopted as the molecules are similar (i.e., $K_{ad,NO_2} = K_{ad,NH_2}$). All values of the adsorption constants $K_{ad,i}$ and the derived partitioning coefficients $K_{part,i}$ are provided in Table S 1 in the Supporting information.

Figure 10 shows that the obtained partitioning coefficients for borohydride, NO_2 , and NH_2 are all decreasing with increasing temperature, as expected for hydrophilic species, which become increasingly expelled from the hydrogel (which becomes hydrophobic above the LCST). NO_2 is undoubtedly deprotonated to 4-nitrophenolate under the experimental conditions where the pH was previously stated to be around 10.⁶⁷ This is a result of the autocatalytic decomposition of borohydride, which slows down exponentially around this pH and remains approximately constant on the timescale of the kinetic measurements. The partitioning coefficient of NH_2 , differing from the behavior of NO_2 , could be a consequence of a slightly higher pH in the range of the dissociation equilibrium of NH_2 (which has a dissociation constant of $pK_a = 10.3$).⁷⁹ As a consequence, not solely NH_2 or 4-aminophenolate would contribute to the observed values, but a mixture of both.

Additionally, Figure 10 shows the partitioning coefficient of NaCl, experimentally determined by Kawasaki et al. between $T = 22$ and 50 °C.⁷⁸ The partitioning coefficient of borohydride is of the same order of magnitude as for NaCl. This fits with the results of Kanduč et al., who found that the partitioning coefficients for small ions are similar, independently of the very type of ion (as the strongly bound hydration shell shields their specific character).⁴¹ Obviously, borohydride is not a simple ion such as chloride, but it is still a monovalent ion with a symmetric charge distribution, and Figure 10 indicates that borohydride exhibits a partitioning coefficient of the same order of magnitude as NaCl.

In contrast to that, the values obtained for NO_2 and NH_2 are markedly higher. The reason for that could be a higher affinity of these organic molecules to the PNIPAM chains of the hydrogel, compared to small ions, which was shown in molecular dynamics simulations of the solute binding affinities to single PNIPAM chains, both for NO_2 and NH_2 .⁸⁰

It can be speculated that a sigmoidal decay of the partitioning coefficients of borohydride, NO_2 , and NH_2 in Figure 10, with an inflection point around the LCST (similar to the hydrodynamic radius in Figure 4), would be more likely than the observed course. However, regarding the assumptions which were made to derive the partitioning coefficients and the complexity of the underlying kinetic model, a further interpretation is problematic.

As a consequence of the results in this chapter, the following implications on the previous chapter arise:

The comparison of the value of K_{ad',BH_4} to the value K_{ad,BH_4} obtained on gold, remains approximately valid as $K_{ad',BH_4} \sim K_{ad,BH_4}$ at $T = 20$ °C. For the case $k_a \ll k_b$, the higher value of K_{ad',NO_2} to the literature value K_{ad,NO_2} , obtained on gold, could be caused by a substantial influence of the partitioning coefficient K_{part,NO_2} which is included in K_{ad',NO_2} .

Overall, the model draws a consistent picture and shows insightful trends against temperature, though some information cannot be derived due to mathematical limitations and unavailable values for the solute partitioning in PNIPAM/adsorption on silver. For an improved analysis, the partitioning coefficients for NO_2 , NH_2 , and borohydride should be included additionally. However, the inclusion as additional fit parameters is impossible as one fit parameter would be replaced by two, and the model would become underdetermined. An alternative could be to use experimentally determined partitioning coefficients; however, to our best knowledge, no studies thereof exist yet.

Conclusion

With the combination of a profound analysis of the reduction of NO_2 with borohydride, catalyzed by silver nanoparticles embedded in core-shell nanoreactors with a thermoresponsive PNIPAM hydrogel shell (Ag@PS-PNIPAM) and based on the decomposition of UV-Vis spectra (with the Levenberg-Marquardt-algorithm), this work covers three major aspects which are generally relevant beyond the very system investigated in this comprehensive kinetic study.

- The potential of the LMA as an assessment tool for the fulfillment of the prerequisites for model reactions as well as for the investigation of the kinetics of reactions with multiple reaction steps was demonstrated. With the reduction of NO_2 on silver, we showed how the LMA can be used to gain essential information about the reaction kinetics, which can then be used to improve or set up a kinetic model. In this work, the LMA showed that no reaction intermediates accumulate in solution, the reactant NO_2 , is directly transferred to the product NH_2 , and a stationary state for the intermediate is present from the beginning of the reaction onwards. The reaction cleanly follows the *direct route* and all intermediates remain adsorbed. This information serves to set up the kinetic model for the reduction of NO_2 on silver subsequently.

- The kinetics of the NO_2 reduction with borohydride on silver was investigated and compared to the kinetics on gold. As this reaction is one of the most widely applied model reactions, detailed information about the reaction kinetics and their differences on different catalyst metals provides useful information for the comparison of kinetic data between different catalyst metals. Here, the analysis showed that the kinetic model differs for the reduction catalyzed by gold and silver, respectively. We presented a two-step Langmuir-Hinshelwood model for the kinetic analysis on silver and applied it to fit the kinetic data. The results reveal a good fit quality and draw a consistent picture of the kinetics, in accordance with results previously

obtained on gold. Furthermore, the analysis showed that the adsorption of the reaction product NH_2 has a considerable influence on the kinetics and should be accounted for in the reduction on silver.

- PNIPAM is under intense research as material for catalytic nanomaterials, hence, accounting for solute (i.e., reactant and product) partitioning coefficients inside nanoreactors (which are macroscopically not easily accessible) and their influence on the reaction kinetics is of general importance for the kinetics of PNIPAM-based catalysts as well as for catalysts comprising other thermoresponsive polymers. With the analysis of the reaction, catalyzed inside a thermoresponsive PNIPAM network at different temperatures, we demonstrated the influence of the partitioning coefficients of reactants and product on the reaction kinetics of catalysts embedded in such thermoresponsive hydrogels. In accordance with theoretical studies by Kanduć et al., the analysis of the partitioning coefficients yields a similar behavior of borohydride compared to NaCl as well as a much higher partitioning coefficient of the reactant NO_2 and the product NH_2 in PNIPAM. This means the actual concentrations at the catalyst surface inside PNIPAM nanoreactors are much higher than the macroscopically measured bulk concentrations which is especially important upon comparing the catalytic performance of such catalysts to others.

By the combination of these aspects, we showcased an approach which enables investigating mechanistic aspects to set up a kinetic model, analyzing the reaction kinetics and accounting for additional effects in thermoresponsive hydrogel-based smart nanoreactors in a single approach.

ASSOCIATED CONTENT

Supporting Information: Histogram of the silver nanoparticle size distribution; description of the TGA measurement and calculation of the silver mass fraction of the catalyst; calculation of the silver surface area per unit volume S ; mathematical description of the decomposition algorithm; reference- and residual spectra of the decomposition; kinetic measurement protocol; comparison of the temporal evolution of the NO_2 concentration obtained via LMA/absorbance at 400 nm; derivation of the kinetic model with the adsorption of NH_2 ; description of the genetic fit algorithm and program code; fits with the kinetic model without the adsorption of NH_2 and detailed analysis of the deviation between fit and experimental data; derivation of the partitioning coefficients via adsorption constants of borohydride and NH_2 and tabulated values. This material is available free of charge via the Internet at <http://pubs.acs.org>.

AUTHOR INFORMATION

Corresponding Author

*(S.R.) sebastian.risse@helmholtz-berlin.de

Present Addresses

*(S.R.) Department of Electrochemical Energy Storage, Helmholtz-Zentrum Berlin für Materialien und Energie, Hahn-Meitner-Platz 1, 14109 Berlin, Germany

§(Y.L.) Department of Electrochemical Energy Storage, Helmholtz-Zentrum Berlin für Materialien und Energie, Hahn-Meitner-Platz 1, 14109 Berlin, Germany
Institute of Chemistry, University of Potsdam, 14476 Potsdam, Germany

†(J.D.) Applied Theoretical Physics – Computational Physics, Physikalisches Institut, Albert-Ludwigs-Universität Freiburg, Hermann-Herder-Straße 3, 79104 Freiburg, Germany
Research Group for Simulations of Energy Materials, Helmholtz-Zentrum Berlin für Materialien und Energie, Hahn-Meitner-Platz 1, 14109 Berlin, Germany

‡(M.B.) Institut für Chemie und Biochemie - Organische Chemie, Freie Universität Berlin, Takustrasse 3, 14195 Berlin, Germany

Funding Sources

European Research Council (ERC) under the European Union's Horizon 2020 research and innovation programme (Grant Agreement No. 646659-NANOREACTOR).

The Authors declare no competing financial interest.

ACKNOWLEDGMENT

This project has received funding from the European Research Council (ERC) under the European Union's Horizon 2020 research and innovation programme (Grant Agreement No. 646659-NANOREACTOR for author J.D.).

ABBREVIATIONS

NO_2 , 4-nitrophenol; NH_2 , 4-aminophenol; $HNNH$, 4,4'-dihydroxyazobenzene; NO , 4-nitrosophenol; $NHOH$, 4-hydroxylaminophenol; PS, polystyrene; PNIPAM, poly-*N*-isopropylacrylamide; Bis, *N,N'*-methylenebisacrylamide; KPS, potassium persulfate; SDS, sodium dodecylsulfate; LMA, Levenberg-Marquardt algorithm; TGA, thermogravimetric analysis; DLS, dynamic light scattering; cryo-TEM, cryogenic transmission electron microscopy.

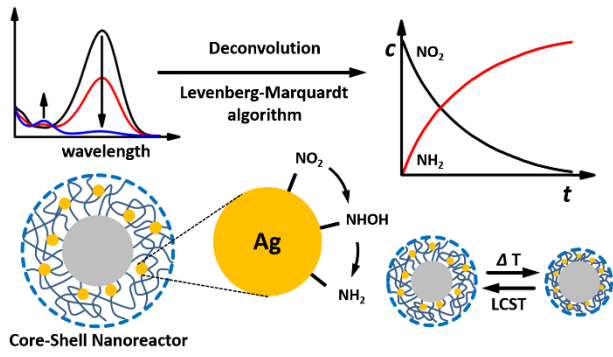
REFERENCES

- (1) *Design of Heterogeneous Catalysts*; Ozkan, U. S., Ed.; Wiley-VCH: Weinheim, 2009.
- (2) Dong, X.-Y.; Gao, Z.-W.; Yang, K.-F.; Zhang, W.-Q.; Xu, L.-W. Nanosilver as a New Generation of Silver Catalysts in Organic Transformations for Efficient Synthesis of Fine Chemicals. *Catal. Sci. Technol.* **2015**, *5*, 2554–2574.
- (3) Polshettiwar, V.; Varma, R. S. Green Chemistry by Nanocatalysis. *Green Chem.* **2010**, *12*, 743–754.
- (4) *Nanoparticles and Catalysis*; Astruc, D., Ed.; Wiley-VCH, 2008.
- (5) Roa, R.; Angioletti-Uberti, S.; Lu, Y.; Dzubiella, J.; Piazza, F.; Ballauff, M. Catalysis by Metallic Nanoparticles in Solution: Thermosensitive Microgels as Nanoreactors. *Z. Phys. Chem.* **2018**, *232*, 773–803.
- (6) Herves, P.; Perez-Lorenzo, M.; Liz-Marzan, L. M.; Dzubiella, J.; Lu, Y.; Ballauff, M. Catalysis by Metallic Nanoparticles in Aqueous Solution: Model Reactions. *Chem. Soc. Rev.* **2012**, *41*, 5577–5587.
- (7) Najeeb, J.; Ahmad, G.; Nazir, S.; Naseem, K.; Kanwal, A. Critical Analysis of Various Supporting Mediums Employed for the Incapacitation of Silver Nanomaterial for Aniline and Phenolic Pollutants: A Review. *Korean J. Chem. Eng.* **2017**, *1–16*.
- (8) Na, K.; Zhang, Q.; Somorjai, G. A. Colloidal Metal Nanocatalysts: Synthesis, Characterization, and Catalytic Applications. *J. Clust. Sci.* **2013**, *25*, 83–114.
- (9) Pushkarev, V. V.; Zhu, Z.; An, K.; Hervier, A.; Somorjai, G. A. Monodisperse Metal Nanoparticle Catalysts: Synthesis,

- Characterizations, and Molecular Studies under Reaction Conditions. *Top. Catal.* **2012**, *55*, 1257–1275.
- (10) Louis, C.; Pluchery, O. *Gold Nanoparticles for Physics, Chemistry and Biology*; Imperial College Press: London, 2012.
- (11) Zahmakiran, M.; Ozkar, S. Metal Nanoparticles in Liquid Phase Catalysis; from Recent Advances to Future Goals. *Nanoscale* **2011**, *3*, 3462–3481.
- (12) Begum, R.; Rehan, R.; Farooqi, Z. H.; Butt, Z.; Ashraf, S. Physical Chemistry of Catalytic Reduction of Nitroarenes Using Various Nanocatalytic Systems: Past, Present, and Future. *J. Nanopart. Res.* **2016**, *18*, 231.
- (13) Ciganda, R.; Li, N.; Deraedt, C.; Gatard, S.; Zhao, P.; Salmon, L.; Hernandez, R.; Ruiz, J.; Astruc, D. Gold Nanoparticles as Electron Reservoir Redox Catalysts for 4-Nitrophenol Reduction: A Strong Stereoelectronic Ligand Influence. *Chem. Commun.* **2014**, *50*, 10126–10129.
- (14) Biondi, I.; Laurency, G.; Dyson, P. J. Synthesis of Gold Nanoparticle Catalysts Based on a New Water-Soluble Ionic Polymer. *Inorg. Chem.* **2011**, *50*, 8038–8045.
- (15) Zhang, L.; Liu, X.; Wang, Y.; Xing, S. Controllable Silver Embedding into Polypyrrole. *J. Alloy Compd.* **2017**, *709*, 431–437.
- (16) Noh, J.-H.; Meijboom, R. Synthesis and Catalytic Evaluation of Dendrimer-Templated and Reverse Microemulsion Pd and Pt Nanoparticles in the Reduction of 4-Nitrophenol: The Effect of Size and Synthetic Methodologies. *Appl. Catal. A* **2015**, *497*, 107–120.
- (17) Bingwa, N.; Meijboom, R. Evaluation of Catalytic Activity of Ag and Au Dendrimer-Encapsulated Nanoparticles in the Reduction of 4-Nitrophenol. *J. Mol. Catal. A* **2015**, *396*, 1–7.
- (18) Antonels, N. C.; Meijboom, R. Preparation of Well-Defined Dendrimer Encapsulated Ruthenium Nanoparticles and Their Evaluation in the Reduction of 4-Nitrophenol According to the Langmuir-Hinshelwood Approach. *Langmuir* **2013**, *29*, 13433–13442.
- (19) Li, S.; Lin, D.; Zhou, J.; Zha, L. Preparation of Silver Nanoparticles Loaded Photoresponsive Composite Microgels and Their Light-Controllable Catalytic Activit. *J. Phys. Chem. C* **2016**, *120*, 4902–4908.
- (20) Liu, G.; Wang, D.; Zhou, F.; Liu, W. Electrostatic Self-assembly of Au Nanoparticles onto Thermosensitive Magnetic Core-shell Microgels for Thermally Tunable and Magnetically Recyclable Catalysis. *Small* **2015**, *11*, 2807–2816.
- (21) Ai, L.; Yue, H.; Jiang, J. Environmentally Friendly Light-Driven Synthesis of Ag Nanoparticles in Situ Grown on Magnetically Separable Biohydrogels as Highly Active and Recyclable Catalysts for 4-Nitrophenol Reduction. *J. Mater. Chem.* **2012**, *22*, 23447–23453.
- (22) Chen, Z.; Cui, Z. M.; Cao, C. Y.; He, W. D.; Jiang, L.; Song, W. G. Temperature-Responsive Smart Nanoreactors: Poly(N-Isopropylacrylamide)-Coated Au@mesoporous-SiO₂ Hollow Nanospheres. *Langmuir* **2012**, *28*, 13452–13458.
- (23) Shifrina, Z. B.; Matveeva, V. G.; Bronstein, L. M. Role of Polymer Structures in Catalysis by Transition Metal and Metal Oxide Nanoparticle Composites. *Chem. Rev.* **2020**, *120*, 1350–1396.
- (24) Dupin, D.; Fujii, S.; Armes, S. P. Efficient Synthesis of Sterically Stabilized PH-Responsive Microgels of Controllable Particle Diameter by Emulsion Polymerization. *Langmuir* **2006**, *22*, 3381–3387.
- (25) Liu, S.; Weaver, J. V. M.; Save, M.; Armes, S. P. Synthesis of PH-Responsive Shell Cross-Linked Micelles and Their Use as Nanoreactors for the Preparation of Gold Nanoparticles. *Langmuir* **2002**, *18*, 8350–8357.
- (26) Nayak, S.; Lyon, L. A. Photoinduced Phase Transitions in Poly (N-Isopropylacrylamide) Microgels. *Chem. Mater.* **2004**, *16*, 2623–2627.
- (27) Wu, Q.; Cheng, H.; Chang, A.; Xu, W.; Lu, F.; Wu, W. Glucose-Mediated Catalysis of Au Nanoparticles in Microgels. *Chem. Commun.* **2015**, *51*, 16068–16071.
- (28) Wu, S.; Dzubiella, J.; Kaiser, J.; Drechsler, M.; Guo, X.; Ballauff, M.; Lu, Y. Thermosensitive Au-PNIPAA Yolk-Shell Nanoparticles with Tunable Selectivity for Catalysis. *Angew. Chem. Int. Ed.* **2012**, *51*, 2229–2233.
- (29) Shah, L. A.; Sayed, M.; Siddiq, M. Fabrication of Ag and Au Nanoparticles in Cross-Linked Polymer Microgels for Their Comparative Catalytic Study. *Mater. Sci. Pol.* **2017**, *35*, 651–659.
- (30) Lanzalaco, S.; Armelin, E. Poly (N-Isopropylacrylamide) and Copolymers: A Review on Recent Progresses in Biomedical Applications. *Gels* **2017**, *3*, 36.
- (31) M. Karg, T. H. Smart Inorganic/Organic Hybrid Microgels: Synthesis and Characterisation. *J. Mater. Chem.* **2009**, *19*, 8714–8727.
- (32) de Las Heras Alarcón, C.; Pennadam, S.; Alexander, C. Stimuli Responsive Polymers for Biomedical Applications. *Chem. Soc. Rev.* **2005**, *34*, 276–285.
- (33) *Metal Nanoparticles for Catalysis*; Tao, F., Ed.; The Royal Society of Chemistry: Cambridge, 2014.
- (34) Roy, D.; Brooks, W. L.; Sumerlin, B. S. New Directions in Thermoresponsive Polymers. *Chem. Soc. Rev.* **2013**, *42*, 7214–7243.
- (35) Fujishige, S.; Kubota, K.; Ando, I. Phase Transition of Aqueous Solutions of Poly (N-Isopropylacrylamide) and Poly (N-Isopropylmethacrylamide). *J. Phys. Chem.* **1989**, *93*, 3311–3313.
- (36) Shi, S.; Wang, Q.; Wang, T.; Ren, S.; Gao, Y.; Wang, N. Thermo-, PH-, and Light-Responsive Poly(N-Isopropylacrylamide-Co-Methacrylic Acid)-Au Hybrid Microgels Prepared by the in Situ Reduction Method Based on Au-Thiol Chemistry. *J. Phys. Chem. B* **2014**, *118*, 7177–7186.
- (37) Kanduč, M.; Kim, W. K.; Roa, R.; Dzubiella, J. Modeling of Stimuli-Responsive Nanoreactors: Rational Rate Control towards the Design of Colloidal Enzymes. *Mol. Sys. Des. Eng.* **2020**, *5*, 602–619.
- (38) Angioletti-Uberti, S.; Lu, Y.; Ballauff, M.; Dzubiella, J. Theory of Solvation-Controlled Reactions in Stimuli-Responsive Nanoreactors. *J. Phys. Chem. C* **2015**, *119*, 15723–15730.
- (39) Galanti, M.; Fanelli, D.; Angioletti-Uberti, S.; Ballauff, M.; Dzubiella, J.; Piazza, F. Reaction Rate of a Composite Core-Shell Nanoreactor with Multiple Nanocatalysts. *Phys. Chem. Chem. Phys.* **2016**, *18*, 20758–20767.
- (40) Roa, R.; Kim, W. K.; Kanduč, M.; Dzubiella, J.; Angioletti-Uberti, S. Catalyzed Bimolecular Reactions in Responsive Nanoreactors. *ACS Catal.* **2017**, *7*, 5604–5611.
- (41) Kanduč, M.; Kim, W. K.; Roa, R.; Dzubiella, J. Aqueous Nanoclusters Govern Ion Partitioning in Dense Polymer Membranes. *ACS Nano* **2019**, *13*, 11224–11234.
- (42) Pradhan, N.; Pal, A.; Pal, T. Catalytic Reduction of Aromatic Nitro Compounds by Coinage Metal Nanoparticles. *Langmuir* **2001**, *17*, 1800–1802.
- (43) Esumi, K.; Miyamoto, K.; Yoshimura, T. Comparison of PAMAM-Au and PPI-Au Nanocomposites and Their Catalytic Activity for Reduction of 4-Nitrophenol. *J. Colloid Interf. Sci.* **2002**, *254*, 402–405.
- (44) Saha, S.; Pal, A.; Kundu, S.; Basu, S.; Pal, T. Photochemical Green Synthesis of Calcium-Alginate-Stabilized Ag and Au Nanoparticles and Their Catalytic Application to 4-Nitrophenol Reduction. *Langmuir* **2010**, *26*, 2885–2893.
- (45) Mahmoud, M. A.; Garlyyev, B.; El-Sayed, M. A. Determining the Mechanism of Solution Metallic Nanocatalysis with Solid and Hollow Nanoparticles: Homogeneous or Heterogeneous. *J. Phys. Chem. C* **2013**, *117*, 21886–21893.
- (46) Haber, F. Über Stufenweise Reduktion Des Nitrobenzols Mit Begrenztem Kathodenpotential. *Z. Electrochem.* **1898**, *4*, 506–514.
- (47) Blaser, H.-U. A Golden Boost to an Old Reaction. *Science* **2006**, *313*, 312–313.
- (48) Levenberg, K. A Method for the Solution of Certain Non-Linear Problems in Least Squares. *Q. Appl. Math.* **1944**, *2*, 164–168.
- (49) Marquardt, D. W. An Algorithm for Least-Squares Estimation

- of Nonlinear Parameters. *J. Soc. Indust. Appl. Math.* **1963**, *11*, 431–441.
- (50) Gavin, H. *The Levenberg-Marquardt Method for Nonlinear Least Squares Curve-Fitting Problems*; Department of Civil and Environmental Engineering, Duke University: Durham, NC, 2015.
- (51) Gu, S.; Wunder, S.; Lu, Y.; Ballauff, M.; Fenger, R.; Rademann, K.; Jaquet, B.; Zaccone, A. Kinetic Analysis of the Catalytic Reduction of 4-Nitrophenol by Metallic Nanoparticles. *J. Phys. Chem. C* **2014**, *118*, 18618–18625.
- (52) Gu, S.; Kaiser, J.; Marzun, G.; Ott, A.; Lu, Y.; Ballauff, M.; Zaccone, A.; Barcikowski, S.; Wagener, P. Ligand-Free Gold Nanoparticles as a Reference Material for Kinetic Modelling of Catalytic Reduction of 4-Nitrophenol. *Catal. Lett.* **2015**, *145*, 1105–1112.
- (53) Gu, S.; Lu, Y.; Kaiser, J.; Albrecht, M.; Ballauff, M. Kinetic Analysis of the Reduction of 4-Nitrophenol Catalyzed by Au/Pd Nanoalloys Immobilized in Spherical Polyelectrolyte Brushes. *Phys. Chem. Chem. Phys.* **2015**, *17*, 28137–28143.
- (54) Hays, J. T.; De Butts, E. H.; Young, H. L. P-Nitrosophenol Chemistry. I. Etherification of p-Nitrosophenol. *J. Org. Chem.* **1967**, *32*, 153–158.
- (55) Lu, Y.; Mei, Y.; Drechsler, M.; Ballauff, M. Thermosensitive Core-Shell Particles as Carriers for Ag Nanoparticles: Modulating the Catalytic Activity by a Phase Transition in Networks. *Angew. Chem. Int. Ed.* **2006**, *45*, 813–816.
- (56) Dingenouts, N.; Norhausen, C.; Ballauff, M. Observation of the Volume Transition in Thermosensitive Core-Shell Latex Particles by Small-Angle X-Ray Scattering. *Macromolecules* **1998**, *31*, 8912–8917.
- (57) Mastronarde, D. N. Automated Electron Microscope Tomography Using Robust Prediction of Specimen Movements. *J. Struct. Biol.* **2005**, *152*, 36–51.
- (58) Liu, J.; Wang, J.; Wang, Y.; Liu, C.; Jin, M.; Xu, Y.; Li, L.; Guo, X.; Hu, A.; Liu, T.; Lincoln, S. F.; Prud'homme, R. K. A Thermosensitive Hydrogel Carrier for Nickel Nanoparticles. *Coll. Interf. Sci. Commun.* **2015**, *4*, 1–4.
- (59) Zhang, J.-T.; Wei, G.; Keller, T. F.; Gallagher, H.; Stötzel, C.; Müller, F. A.; Gottschaldt, M.; Schubert, U. S.; Jandt, K. D. Responsive Hybrid Polymeric/Metallic Nanoparticles for Catalytic Applications. *Macromol. Mater. Eng.* **2010**, *295*, 1049–1057.
- (60) Liang, M.; Zhang, G.; Feng, Y.; Li, R.; Hou, P.; Zhang, J.; Wang, J. Facile Synthesis of Silver Nanoparticles on Amino-Modified Cellulose Paper and Their Catalytic Properties. *J. Mater. Sci.* **2017**, *53*, 1568–1579.
- (61) Shabir, J.; Rani, S.; Garkoti, C.; Mozumdar, S. Nitrolotriactic Acid Assisted One Step Synthesis of Highly Stable Silver Nanoparticles in Aqueous Medium: Investigation of Catalytic Activity. *Mater. Lett.* **2017**, *209*, 207–211.
- (62) Kästner, C.; Thünemann, A. F. Catalytic Reduction of 4-Nitrophenol Using Silver Nanoparticles with Adjustable Activity. *Langmuir* **2016**, *32*, 7383–7391.
- (63) Bano, M.; Ahirwar, D.; Thomas, M.; Naikoo, G. A.; Sheikh, M. U.-D.; Khan, F. Hierarchical Synthesis of Silver Monoliths and Their Efficient Catalytic Activity for the Reduction of 4-Nitrophenol to 4-Aminophenol. *New J. Chem.* **2016**, *40*, 6787–6795.
- (64) Corma, A.; Concepción, P.; Serna, P. A Different Reaction Pathway for the Reduction of Aromatic Nitro Compounds on Gold Catalysts. *Angew. Chem. Int. Ed.* **2007**, *46*, 7266–7269.
- (65) Wunder, S.; Polzer, F.; Lu, Y.; Mei, Y.; Ballauff, M. Kinetic Analysis of Catalytic Reduction of 4-Nitrophenol by Metallic Nanoparticles Immobilized in Spherical Polyelectrolyte Brushes. *J. Phys. Chem. C* **2010**, *114*, 8814–8820.
- (66) Rill, C.; Kolar, Z. I.; Kickelbick, G.; Wolterbeek, H. T.; Peters, J. A. Kinetics and Thermodynamics of Adsorption on Hydroxyapatite of the [160Tb] Terbium Complexes of the Bone-Targeting Ligands DOTP and BPPED. *Langmuir* **2009**, *25*, 2294–2301.
- (67) Wunder, S.; Lu, Y.; Albrecht, M.; Ballauff, M. Catalytic Activity of Faceted Gold Nanoparticles Studied by a Model Reaction: Evidence for Substrate-Induced Surface Restructuring. *ACS Catal.* **2011**, *1*, 908–916.
- (68) Vannice, M. A. *Kinetics of Catalytic Reactions*; Springer: New York, 2013.
- (69) Glasser, L. Rates of Bimolecular Heterogeneous Reactions Following the Langmuir-Hinshelwood Mechanism. *J. Chem. Educ.* **1979**, *56*, 22–23.
- (70) Sips, R. On the Structure of a Catalyst Surface. *J. Chem. Phys.* **1948**, *16*, 490–495.
- (71) Wu, S.; Kaiser, J.; Guo, X.; Li, L.; Lu, Y.; Ballauff, M. Recoverable Platinum Nanocatalysts Immobilized on Magnetic Spherical Polyelectrolyte Brushes. *Ind. Eng. Chem. Res.* **2012**, *51*, 5608–5614.
- (72) Lu, Y.; Mei, Y.; Ballauff, M. Thermosensitive Core-Shell Particles as Carrier Systems for Metallic Nanoparticles. *J. Phys. Chem. B* **2006**, *110*, 3930–3937.
- (73) Lu, Y.; Yuan, J.; Polzer, F.; Drechsler, M.; Preussner, J. In Situ Growth of Catalytic Active Au-Pt Bimetallic Nanorods in Thermoresponsive Core-Shell Microgels. *ACS Nano* **2010**, *4*, 7078–7086.
- (74) Wedler, G. *Lehrbuch Der Physikalischen Chemie*; Wiley-VCH: Weinheim, 2004.
- (75) Palasis, M.; Gehrke, S. H. Permeability of Responsive Poly (N-Isopropylacrylamide) Gel to Solutes. *J. Control. Release* **1992**, *18*, 1–11.
- (76) Sassi, A. P.; Shaw, A. J.; Han, S. M.; Blanch, H. W.; Prausnitz, J. M. Partitioning of Proteins and Small Biomolecules in Temperature-and PH-Sensitive Hydrogels. *Polymer (Guildf.)* **1996**, *37*, 2151–2164.
- (77) Gehrke, S. H.; Fisher, J. P.; Palasis, M.; Lund, M. E. Factors Determining Hydrogel Permeability. *Ann. N.-Y. Acad. Sci.* **1997**, *831*, 179–184.
- (78) Kawasaki, H.; Mitou, T.; Sasaki, S.; Maeda, H. Partition of Salts between N-Isopropylacrylamide Gels and Aqueous Solutions. *Langmuir* **2000**, *16*, 1444–1446.
- (79) *CRC Handbook of Chemistry and Physics*; Lide, D. R., Ed.; CRC Press: Boca Raton, 1998.
- (80) Kanduč, M.; Chudoba, R.; Palczynski, K.; Kim, W. K.; Roa, R.; Dzubiella, J. Selective Solute Adsorption and Partitioning around Single PNIPAM Chains. *Phys Chem Chem Phys* **2017**, *19*, 5906–5916.

For table of contents only



Supporting Information:

Kinetics of the reduction of 4-nitrophenol by silver nanoparticles immobilized in thermoresponsive core-shell nanoreactors

Daniel Besold, Sebastian Risse,* Yan Lu,[§] Joachim Dzubiella[†] and Matthias Ballauff[‡]

Soft Matter and Functional Materials, Helmholtz-Zentrum Berlin für Materialien und Energie, Hahn-Meitner-Platz 1, 14109 Berlin, Germany

Characterization

Cryo-TEM

To obtain the size distribution of the silver nanoparticles, about 400 particles were measured with ImageJ v.1.49 (Wayne Rasband, National Institute of Health, USA) in several cryo-TEM images.

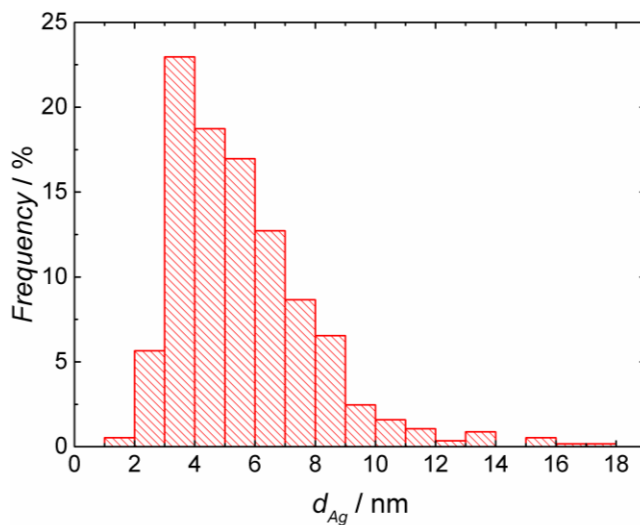


Figure S 1. Histogram of the silver nanoparticles determined from cryo-TEM images.

TGA

The weight loss of the microgels with and without metal nanoparticles was measured, and the residual mass of the pure polymer was considered in the calculation of the metal mass fraction. From the TGA measurement of the PS-PNIPAM nanoreactors before the synthesis of silver nanoparticles, the relative mass loss of the pure polymer $f_{loss,-}$ was obtained. The TGA measurement of the Ag@PS-PNIPAM nanoreactors after the synthesis of metal nanoparticles yielded a relative mass loss $f_{loss,+}$ which was only caused by the mass loss of the polymer. From the ratio of the latter and $f_{loss,-}$, the polymer mass fraction of the nanoreactor was obtained, and the silver mass fraction f_{Ag} of the nanoreactor was calculated according to

$$f_{Ag} = 1 - \frac{f_{loss,+}}{f_{loss,-}}, \quad (S 1)$$

yielding $f_{Ag} = 0.099$.

Calculation of the surface area per unit volume S

The silver surface area to mass ratio of the nanoparticles $r_{A/m}$, with units of $[\text{m}^2 \text{g}^{-1}]$, is required to determine the metal surface area per unit volume S . The latter can be calculated with the diameter of the metal nanoparticles $d_{Ag} = 2 r_{Ag} = 5.6 \pm 2.4 \text{ nm}$ and the density of silver ($\rho_{Ag} = 10.49 \times 10^6 \text{ g m}^{-3}$)¹ according to

$$r_{A/m} = \frac{A_{Ag}}{V_{Ag} \rho_{Ag}} = \frac{4 \pi r_{Ag}^2}{\frac{4}{3} \pi r_{Ag}^3 \rho_{Ag}} = \frac{3}{r_{Ag} \rho_{Ag}}, \quad (S 2)$$

where A_{Ag} is the surface area of one single nanoparticle and V_{Ag} is its volume. The surface area to mass ratio is multiplied by the mass concentration of the Ag@PS-PNIPAM stock catalyst suspension $c_m = 0.194 \text{ g L}^{-1}$, and the silver fraction of the nanoreactors f_{Ag} , according to

$$S = r_{A/m} f_{Ag} c_m, \quad (S 3)$$

yielding a metal surface area per unit volume of $S = 2.0 \text{ m}^2 \text{ L}^{-1}$ for the catalyst stock suspension.

Spectral decomposition

Decomposition algorithm

The overall absorption $A_{model}(\lambda_i)$, at one of the n wavelengths λ_i and at a specific time t during the reduction of NO_2 , is a superposition of the following absorption contributions

$$\begin{aligned} A_{model}(\lambda_i) = & c_{\text{NO}_2}(t)E_{\text{NO}_2}(\lambda_i) + c_{\text{NH}_2}(t)E_{\text{NH}_2}(\lambda_i) + c_{\text{NO}}(t)E_{\text{NO}}(\lambda_i) + \\ & + c_{\text{HNNH}}(t)E_{\text{HNNH}}(\lambda_i) + c_{\text{cat}}(t)E_{\text{cat}}(\lambda_i) + \underbrace{\sum_{k=1}^{n-5} a_k \frac{\text{Exp}\left[-\frac{(\lambda_k - \lambda_i)^2}{2\sigma^2}\right]}{\sqrt{2\pi\sigma^2}}}_{A_{res}(\lambda_i)}. \end{aligned} \quad (S 4)$$

Here $E_j(\lambda_i)$ and $c_j(t)$ are the respective extinction curves and concentrations of the reference species, respectively. The last term $A_{res}(\lambda_i)$ describes the residual spectra of unknown species and consists of a sum of Gaussian distributions with a standard deviation $\sigma = 1$ nm and different amplitudes a_k . Therefore, the whole absorption spectrum $A_{model}(\lambda_i)$ can be regarded as a vector $\vec{A}_{model}(\vec{\beta})$, dependent on the fit parameter vector $\vec{\beta}$, which has to be fitted to the data vector \vec{A}_{data} . The fit parameter vector is defined as

$$\vec{\beta}^T = (c_{NO_2}, c_{NH_2}, c_{NO}, c_{HNNH}, c_{cat}, a_1, \dots, a_{n-5}). \quad (S 5)$$

The different λ_k of the residual spectrum range from $\lambda_1 - 5\sigma$ up to $\lambda_n + 5\sigma$ in equidistant $n - 5$ steps. This specific range ensures that also the contribution of unknown species that are slightly outside of the observed wavelength interval can contribute to the overall absorption. A modified Levenberg-Marquardt algorithm with a damping parameter $\lambda_d = 1$ was implemented in Mathematica (Wolfram Research) to find the fit parameters for each time t with

$$(\mathbf{J}^T \mathbf{J} + \lambda_d \cdot \text{diag}(\mathbf{J}^T \mathbf{J})) \cdot \mathbf{D} \cdot \vec{\delta} = \mathbf{J}^T (|\vec{A}_{data} - \vec{A}_{model}(\vec{\beta})|), \quad (S 6)$$

where \mathbf{J} is the Jacobi matrix, defined as

$$\mathbf{J} = \frac{\partial \vec{A}_{model}(\vec{\beta})}{\partial \vec{\beta}}, \quad (S 7)$$

\mathbf{D} is the weighting matrix, and $\vec{\delta}$ is an n-dimensional step vector.

The differentiation with respect to the fit parameters $\vec{\beta}$ gives

$$\mathbf{J}_{ij} = \begin{cases} j = 1: & E_{NO_2}(\lambda_i) \\ j = 2: & E_{NH_2}(\lambda_i) \\ j = 3: & E_{NO}(\lambda_i) \\ j = 4: & E_{HNNH}(\lambda_i) \\ j = 5: & E_{cat}(\lambda_i) \\ \text{else:} & \mathbf{A}_{res,ij} \end{cases}. \quad (S 8)$$

The weighting matrix

$$\mathbf{D}_{ii} = \begin{cases} 10^4 & \text{for } i \leq 5 \\ 1 & \text{else} \end{cases} \quad (S 9)$$

has only non-zero entries on the main diagonal and prioritizes the fit with the extinction curves $E_j(\lambda_i)$ over the residual spectrum $A_{res}(\lambda_i)$.

The n-dimensional step vector

$$\vec{\delta} = \left((\mathbf{J}^T \mathbf{J} + \lambda_d \cdot \text{diag}(\mathbf{J}^T \mathbf{J})) \cdot \mathbf{D} \right)^{-1} \mathbf{J}^T (|\vec{A}_{data} - \vec{A}_{model}(\vec{\beta})|) \quad (S 10)$$

can be calculated in each iteration step and gives a new adjusted parameter vector

$$\vec{\beta}_{new} = |\vec{\beta} + \vec{\delta}|. \quad (S 11)$$

The entries of the initial parameter vector $\vec{\beta}_{start}$ at each time t were set as

$$\vec{\beta}_{start}^T = (c_{NO_2}, c_{NH_2}, 0.01 \mu M, 0.01 \mu M, c_{cat}, 0.01 \mu M \cdot nm, \dots, 0.01 \mu M \cdot nm), \quad (S 12)$$

$$c_{NO_2} = \frac{A_{data}(400\text{ nm})|_t}{E_{NO_2}(400\text{ nm})}, \quad (\text{S } 13)$$

and

$$c_{NH_2} = \frac{A_{data}(400\text{ nm})|_{t=0}}{E_{NO_2}(400\text{ nm})} - \frac{A_{data}(400\text{ nm})|_t}{E_{NO_2}(400\text{ nm})}. \quad (\text{S } 14)$$

The fit routine was stopped after 10^6 iterations and the concentrations of each reference species at time $t = t_0$, as well as the residual spectrum, was extracted from the last parameter vector $\vec{\beta}$.

Details of the decomposition

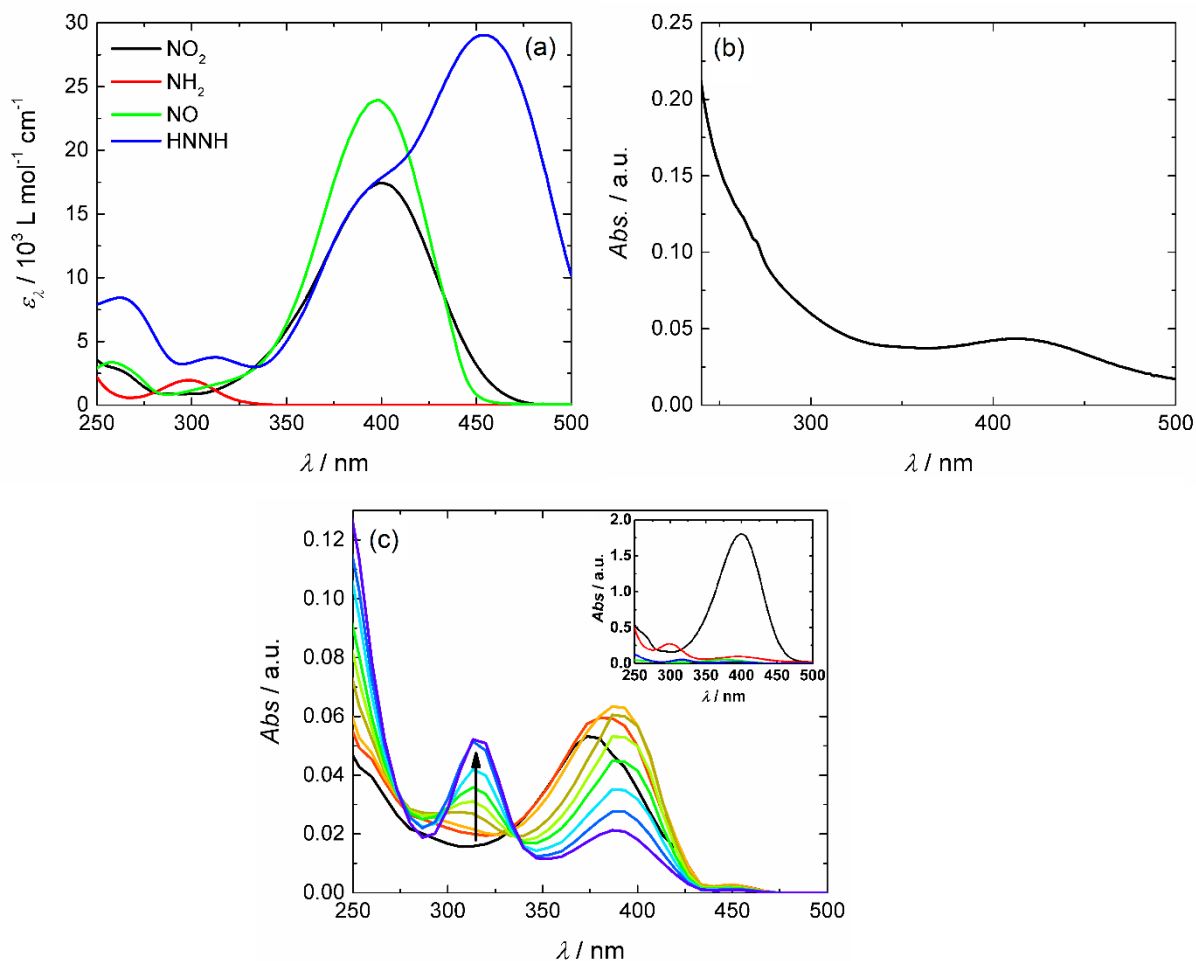


Figure S 2. Spectra of the molar extinction coefficient (a) for NO_2 , NH_2 , NO and $HNNH$ recorded at $pH = 10$, spectrum of the catalyst (b), recorded at a surface area per unit volume of $S = 0.0625 \text{ m}^2 \text{ L}^{-1}$ which was used for the kinetic measurements, and obtained residual spectra upon decomposition (c). The inset shows the first (black) and last (red) spectrum recorded during the reduction compared to the corresponding first (green) and last (blue) residual spectrum.

Figure S 2 (a) shows the spectra of the molar extinction coefficient ϵ_λ for the reactant NO_2 , the product NH_2 , one intermediate of the direct route NO , and one intermediate of the condensation route $HNNH$ which were used as reference spectra for the decomposition. Figure S 2 (b) shows the absorbance of the catalyst at the concentration which was applied in the kinetic measurements. Figure S 2 (c) shows the residual spectra obtained upon decomposition of the spectra in Figure 5 (a). The spectra show an overall low intensity compared to the experimental spectra, as shown in the inset.

Kinetic measurement protocol

Dry borohydride was prepared in a small vial under N_2 atmosphere to prevent the uptake of humidity (due to its hygroscopicity) for each measurement. Millipore water and a 4-nitrophenol (NO_2) stock solution ($c_{NO_2} = 0.01 \text{ mol L}^{-1}$) were degassed and subsequently held under N_2 atmosphere. Shortly before the reactants were mixed, borohydride was dissolved in degassed water to yield $c_{BH_4} = 0.05 \text{ mol L}^{-1}$ and held under N_2 atmosphere.

For a typical run, the reaction mixture was prepared directly in the cuvette. The cuvette was placed inside the thermostatted cuvette holder ($\Delta T \leq 0.1 \text{ }^\circ\text{C}$) and constantly purged with N_2 (above the liquid surface) to prevent oxygen uptake. First, water and the desired amount of NO_2 stock solution were added to the cuvette, followed by the corresponding amount of borohydride. After that, the catalyst was added, the N_2 purge was removed, and the cuvette was simultaneously sealed. The cuvette was turned once for mixing, and the measurement was initiated immediately. Like that, the delay between adding the catalyst (i.e. start of the reaction) and start of the measurement could be kept below 5 seconds. All experiments were carried out three times and averaged to obtain more reliable results. Spectra were recorded every 5 seconds, and the time dependency of the NO_2 concentration was derived from the absorption at $\lambda = 400 \text{ nm}$.

All measurements were performed at a silver surface area per unit volume of $S = 0.0625 \text{ m}^2 \text{ L}^{-1}$, and with a measurement volume of 3 mL. For the measurements against temperature, the reaction mixture was thermostatted for three minutes before addition of the catalyst and initiation of the measurement.

Kinetic analysis

Comparison of the temporal evolution of the NO_2 concentration

Figure S 3 shows that the temporal evolution of the NO_2 concentration obtained via spectral decomposition with the Levenberg-Marquardt algorithm is virtually identical to the concentration obtained from the optical (UV-Vis) absorption at $\lambda = 400 \text{ nm}$. Therefore, the latter can be used for the kinetic evaluation.

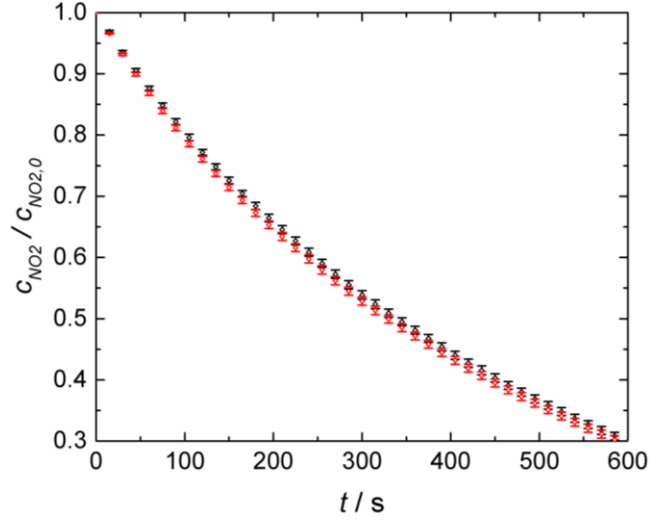


Figure S 3. Comparison of the NO_2 concentration obtained via spectral decomposition (black) and obtained from the optical absorption at $\lambda = 400$ nm (red).

Derivation of the kinetic model including the adsorption of NH_2

The kinetic model can be derived similarly as shown previously without the adsorption of NH_2 .^{2,3} According to the Langmuir-Hinshelwood model, the temporal evolution of the concentration of NO_2 can be expressed as

$$-\frac{dc_{NO_2}}{dt} = k_a S \theta_{NO_2} \theta_{BH_4}. \quad (S 15)$$

The surface coverages θ_i for NO_2 and borohydride can be derived as

$$\theta_i = \frac{K_{ad,i} c_i}{\left(1 + (K_{ad,NO_2} c_{NO_2})^n + K_{ad,NHOH} c_{NHOH} + K_{ad,BH_4} c_{BH_4} + K_{ad,NH_2} c_{NH_2}\right)} \quad (S 16)$$

and equation (S 15) is obtained as equation 2 in the main text:

$$-\frac{dc_{NO_2}}{dt} = \frac{k_a S (K_{ad,NO_2} c_{NO_2})^n K_{ad,BH_4} c_{BH_4}}{\left(1 + (K_{ad,NO_2} c_{NO_2})^n + K_{ad,NHOH} c_{NHOH} + K_{ad,BH_4} c_{BH_4} + K_{ad,NH_2} c_{NH_2}\right)^2}. \quad (S 17)$$

The concentration of NH_2 can be described accordingly with the surface reaction between the reaction intermediate 4-hydroxylaminophenol ($NHOH$) and borohydride with the reaction rate constant k_b of the second reaction step according to

$$\frac{dc_{NH_2}}{dt} = k_b S \theta_{NHOH} \theta_{BH_4} = \frac{k_b S K_{ad,NHOH} c_{NHOH} K_{ad,BH_4} c_{BH_4}}{\left(1 + (K_{ad,NO_2} c_{NO_2})^n + K_{ad,NHOH} c_{NHOH} + K_{ad,BH_4} c_{BH_4} + K_{ad,NH_2} c_{NH_2}\right)^2} \quad (S 18)$$

and the kinetic model can be derived as further described in the main text.

Fit algorithm

The differential equation (S 19) was used to fit the kinetic data by a genetic approach.⁴ The data were fitted with Mathematica (Wolfram Research). Figure S 4 shows the flow chart of the fit algorithm. After

importing the discrete experimental data and transferring them into continuous data with a spline fit, a conversion limit was set up to which the data are fitted. For each parameter p_i , a range was defined, and test parameters were derived in N_i logarithmic equidistant intervals to generate parameter sets which are tested with the target function

$$\varepsilon_j(t_l, s_j) = \frac{1}{2N_{exp}} \left(\sum_1^{N_{exp}} \left(\sum_{t=0}^{t=t_l} \frac{|c_{exp}(t) - c_{fit}(t, s_j)|}{c_{exp}(t)} \right) + \sum_1^{N_{exp}} \left(\sum_{t=0}^{t=t_l} \frac{|c'_{exp}(t) - c'_{fit}(t, s_j)|}{c'_{exp}(t)} \right) \right) \quad (S 19)$$

to derive a reasonable starting parameter set s_j^* for the mutation step. Here, N_{exp} is the number of experimental curves which were fitted simultaneously, t_l is the limiting time of each experimental curve at which the conversion limit is reached, $c_{exp}(t)$, $c_{fit}(t)$, $c'_{exp}(t)$ and $c'_{fit}(t)$ are the experimental and the fitted concentration-time curves and their first derivatives (i.e. the curvature), respectively. In the subsequent mutation step, each fit parameter of s_j^* was randomly varied within the margins of $\Delta p_i \leq \pm 1\%$, and the new parameter set s_j^{**} was tested with the target function $\varepsilon_j(t_l, s_j^{**})$. If its value decreased, compared to the value for $\varepsilon_j(t_l, s_j^*)$, the new parameter set was used in the next mutation cycle, otherwise, the previous set is maintained. This is repeated until no improved set of fit parameters is obtained in $c_n = 200$ consecutive mutation cycles.

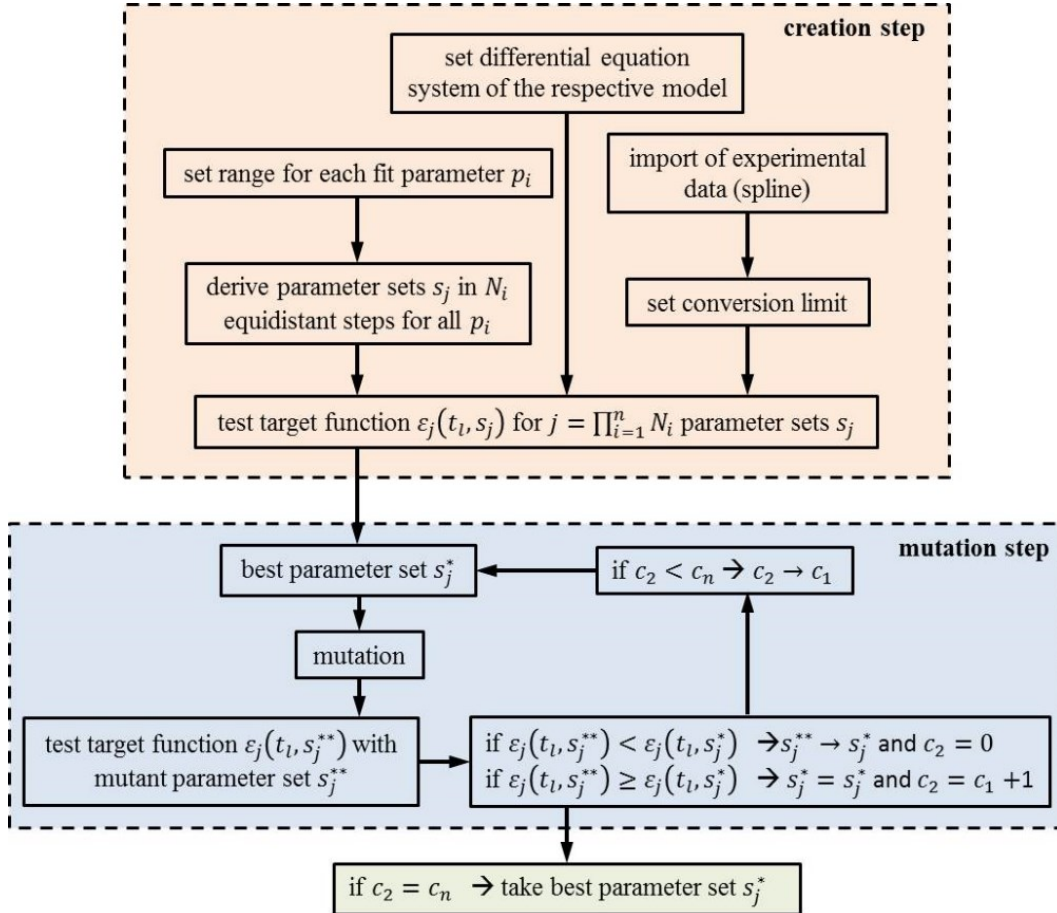


Figure S 4. Flow chart of the genetic fit algorithm. In the creation step a spline fit is used to transfer the discrete experimental data into continuous datasets. The final fit is obtained after no further improvement is achieved in c_n consecutive mutation loops.

The steps of the program code (attached in the following) are as follows:

- 1) Import (discrete) experimental data and transfer into continuous data with a spline fit.
- 2) Define experimental conversion limit to define up to which time t_l the data are fitted.
- 3) Define differential equations and fit parameter p_i for the fit.
- 4) Define range for each fit parameter p_i .
- 5) Set values in N_i equidistant steps for each fit parameter p_i within the respective range and generate starting parameter sets s_j of their combinations.
- 6) Test the starting parameter sets s_j with the target function $\varepsilon_j(t_l, s_j)$ in equation (S 19).
- 7) Take the best parameter set s_j^* (for which $\varepsilon_j(t_l, s_j^*)$ is minimal) and mutate by randomly varying each parameter within the margins of $\Delta p_i \leq \pm 1\%$ to generate mutant parameter set s_j^{**} .
- 8) Test mutant parameter sets s_j^{**} with the target function $\varepsilon_j(t_l, s_j^{**})$.
- 9) If $\varepsilon_j(t_l, s_j^{**}) < \varepsilon_j(t_l, s_j^*)$, take mutant parameter set and repeat mutation cycle, if $\varepsilon_j(t_l, s_j^{**}) \geq \varepsilon_j(t_l, s_j^*)$, keep old parameter set and repeat mutation cycle.
- 10) The final result is obtained if no improved parameter set If $\varepsilon_j(t_l, s_j^{**}) < \varepsilon_j(t_l, s_j^*)$ is obtained for $c_n = 200$ consecutive mutation cycles.

Program code:

```
(*Import step*)
SetDirectory[StringJoin[{NotebookDirectory[], "\\Results"}]];
fn = FileNames["*.txt"];
impNip[x_] := {#[[1]], #[[2]]} & /@ Take[Import[x, "Table"], {2, -1}];
df[y_] :=
  Transpose[{Transpose[y][[1]],
    D[Interpolation[y][x], x] /. x -> Transpose[y][[1]]}];
DATAx = impNip /@ fn;

(*Set conversion limit*)
Xconv = 0.3;

(*Define Differential equations*)
MODEL[x_, cNip0_, cBH4_, n0_, ks_, KNip_, KBH4_] :=
  1/(cBH4 KBH4 ks (-1 + n0) (1 + n0)) cNip0^(1 - n0)
  KNip^-n0 x^-n0 ((-1 + (cNip0 KNip)^n0)^2 + (-1 + (cNip0 KNip)^(
    2 n0)) n0 + 2 (cNip0 KNip)^n0 n0^2 -
  cBH4^2 KBH4^2 (1 + n0) +
  2 cBH4 KBH4 (1 + n0) (-1 - (cNip0 KNip)^
  n0 + (cNip0 KNip)^n0 n0)) x^n0 +
  x (n0 + cBH4^2 KBH4^2 (1 + n0) - 2 n0^2 (cNip0 KNip x)^n0 -
  n0 (cNip0 KNip x)^(2 n0) + (1 + (cNip0 KNip x)^n0)^2 -
  2 cBH4 KBH4 (1 + n0) (-1 - (cNip0 KNip x)^n0 +
  n0 (cNip0 KNip x)^n0));
DMODEL[x_, cNip0_, cBH4_, n0_, ks_, KNip_,
  KBH4_] := -((
```

```
ks cNip0^(n0 - 1) x^n0 KNip^
n0 cBH4 KBH4/(1 + (cNip0 x KNip)^n0 + cBH4 KBH4^2)^-1;
```

```
dDATAx = df /@ (Select[#, 0.9 > #[[2]] > 0.15 &] & /@ DATAx);
strBH4[x_] :=
  ToExpression[
    StringTake[StringCases[x, "-" ~~ __ ~~ "-"][[1]], {2, -2}]];
strNip0[x_] :=
  ToExpression[StringTake[x, {1, StringPosition[x, "-"][[1, 1]] - 1}]];
```

```
cBH4s = N[strBH4 /@ fn*10^-3]
Nip0s = N[10^-3 (strNip0 /@ fn)]
Grid[{{
  ListLinePlot[DATAx, Frame -> True, ImageSize -> 300,
    PlotRange -> Full],
  ListLinePlot[dDATAx, Frame -> True, ImageSize -> 300,
    PlotRange -> Full]}}
```

```
DATAxCut = (Select[#, #[[2]] >= 1 - Xconv &] & /@ DATAx);
dDATAxCut =
  df /@ (Reverse[#] & /@ # & /@ (Select[#, 0.9 >= #[[2]] &] & /@
    DATAxCut));
```

(*Set range of parameters*)

```
{n0min, n0max} = {0.05, 1};
{ksmin, ksmax} = {10^-8, 10^-2};
{KNipmin, KNipmax} = {10^2, 10^6};
{KBH4min, KBH4max} = {10^-3, 10^1};
```

(*Set parameters in equidistant steps*)

```
PARS0 = Flatten[N[Table[{i1, 10^i2, 10^i3, 10^i4},
  {i1, n0min, n0max, (n0max - n0min)/7},
  {i2, Log10[ksmin], Log10[ksmax], (Log10[ksmax] - Log10[ksmin])/7},
  {i3, Log10[KNipmin], Log10[KNipmax], (
    Log10[KNipmax] - Log10[KNipmin])/7},
  {i4, Log10[KBH4min], Log10[KBH4max], (
    Log10[KBH4max] - Log10[KBH4min])/7}], 3];
```

(*Creation step*)

```
n = 0;
Err0 = 10^10;
Dynamic[n]
Dynamic[PARS]
Dynamic[Err0]
Do[
  n = n + 1;
  err = Mean[
    Table[Mean[
      Abs[(MODEL @@
        Flatten[{{#[[2]], Nip0s[[i]], cBH4s[[i]], PARS0[[n]]}}] & /@
        Take[DATAxCut[[i]], {2, -1}] - (#[[1]] & /@
        Take[DATAxCut[[i]], {2, -1}])/#[[1]] & /@
        Take[DATAxCut[[i]], {2, -1}]], {i, 1, Length[fn]}]];
  derr = Mean[
    Table[Mean[
      Abs[(DMODEL @@
        Flatten[{{#[[1]], Nip0s[[i]], cBH4s[[i]], PARS0[[n]]}}] & /@
        Take[dDATAxCut[[i]], {2, -1}] - (#[[2]] & /@
```

```

    Take[dDATAxCut[[i]], {2, -1}))/#[[2]] & /@
    Take[dDATAxCut[[i]], {2, -1}]], {i, 1, Length[fn]]];
Err = Mean[{err, derr};
If[Err < Err0, PARS = PARS0[[n]]; Err0 = Err];
, {Length[PARS0]]

(*Mutation step*)
n = 0;
count = 0;
Dynamic[n]
Dynamic[countMax]
Dynamic[PARS]
Dynamic[Err0]

Do[
n = n + 1;
count = count + 1;
l0 = Length[PARS];
RI = RandomInteger[{1, l0}];
fac = RandomSample[
Join[Table[RandomReal[{0.99, 1.01}], {RI}], Table[1, {l0 - RI}],
l0];
guess = fac*PARS;
err = Mean[
Table[Mean[
Abs[(MODEL @@
Flatten[{#[[2]], Nip0s[[i]], cBH4s[[i]], guess}] & /@
Take[DATAxCut[[i]], {2, -1}] - (#[[1]] & /@
Take[DATAxCut[[i]], {2, -1}))/#[[1]] & /@
Take[DATAxCut[[i]], {2, -1}]], {i, 1, Length[fn]]];
derr = Mean[
Table[Mean[
Abs[(DMODEL @@
Flatten[{#[[1]], Nip0s[[i]], cBH4s[[i]], guess}] & /@
Take[dDATAxCut[[i]], {2, -1}] - (#[[2]] & /@
Take[dDATAxCut[[i]], {2, -1}))/#[[2]] & /@
Take[dDATAxCut[[i]], {2, -1}]], {i, 1, Length[fn]]];
Err = Mean[{err, derr};
If[Err < Err0, PARS = guess; Err0 = Err; countMax = count];
, {100000}]

```

Fits with the kinetic model without the adsorption of NH_2

The equation for the kinetic model without the adsorption of NH_2 was derived previously as³

$$-\frac{dc_{NO_2}}{dt} = \frac{k_a S (K_{ad',NO_2} c_{NO_2})^n K_{ad',BH_4} c_{BH_4}}{\left(1 + \left(1 + \frac{k_a}{k_b}\right) (K_{ad',NO_2} c_{NO_2})^n + K_{ad',BH_4} c_{BH_4}\right)^2} \quad (S\ 20)$$

Equally to the model with the adsorption of NH_2 it is underdetermined and can be rewritten as

$$-\frac{dc_{NO_2}}{dt} = K_1 S \frac{(c_{NO_2})^n K_{ad',BH_4} c_{BH_4}}{\left(1 + K_2 (c_{NO_2})^n + K_{ad',BH_4} c_{BH_4}\right)^2} \quad (S\ 21)$$

The obtained fit results (for the data used for the global fit at $T = 20\text{ }^{\circ}\text{C}$ shown in the main text) in Figure S 5 show that the fits significantly deviate from the experimental data. At higher conversion, the fits begin to deviate towards lower concentrations and the curvature of the fit does not match with the experimental data. Two potential reasons for the deviation are conceivable: A decrease in the borohydride concentration due to its partial decomposition during the reaction time, and the adsorption of the reaction product NH_2 to the catalyst surface. Both effects are not captured by the model. To assess which of the two potential reasons is more probable, the deviation relative to the absolute NO_2 concentration at each time t is analyzed and discussed in the following.

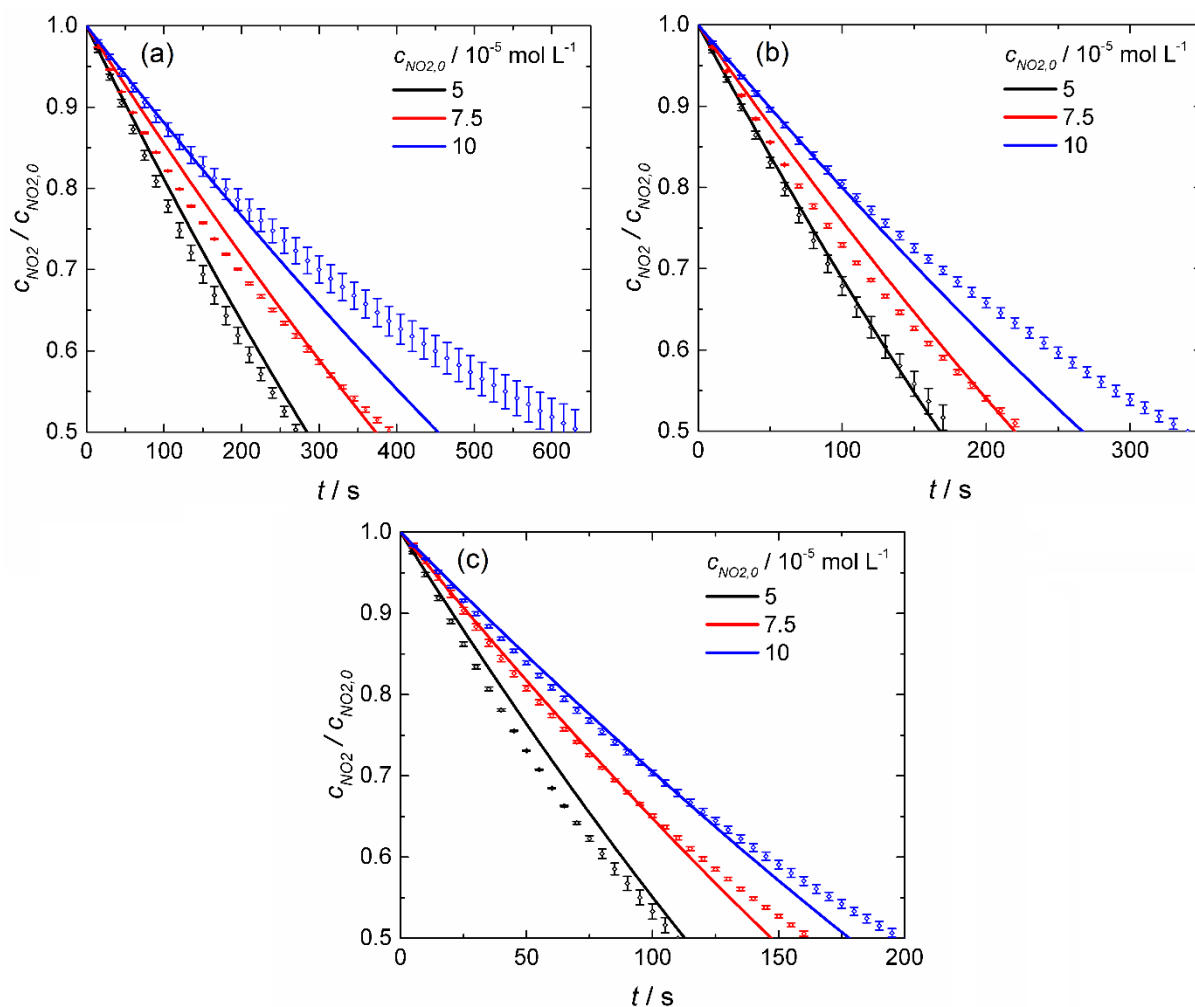


Figure S 5. Time dependencies of the experimental NO_2 concentration (symbols) and fit results for the kinetic model without the adsorption of NH_2 (lines) for the reduction at $c_{\text{BH}_4} = 5 \times 10^{-3}$ (a), 1×10^{-2} (b), and $2 \times 10^{-2} \text{ mol L}^{-1}$ (c).

Deviation of the fit without product adsorption from the experimental data

To evaluate the difference between fitted and experimental curves of the NO_2 concentration at $T = 20\text{ }^{\circ}\text{C}$, the relative residue is calculated according to

$$\Delta(c_{exp} - c_{fit})_{rel} = \frac{c_{exp}(t) - c_{fit}(t)}{c_{exp}(t)} = 1 - \frac{c_{fit}(t)}{c_{exp}(t)}. \quad (\text{S } 22)$$

With equation (S 22), the deviation between fit and experiment can be evaluated relative to the absolute NO_2 concentration at the respective time and independently of the initial concentration. This way, a comparison of the deviation between the different experiments at $T = 20\text{ }^\circ\text{C}$ is possible. Furthermore, the deviation is plotted against conversion instead of reaction time as the data are always fitted up to 50% conversion (which is reached at different times for each experiment).

To evaluate whether the deviation may be caused by a decrease in the borohydride concentration (due to hydrolysis) or by adsorption of NH_2 , the deviation graphs are plotted in two ways. Figure S 6 (a), (c) and (e) each show the three measurements at equal NO_2 and varying borohydride concentration while Figure S 6 (b), (d) and (f) compare measurements at equal borohydride and varying NO_2 concentration.

The hydrolysis of borohydride is catalyzed by protons, i.e. pH -dependent. Upon decomposition, the pH increases, and the rate of hydrolysis is therefore fast at the beginning and becomes exponentially slower with time as the pH increases.⁵ However, as the reaction volume is the same for all experiments, the same amount of borohydride will be hydrolyzed in all experiments before the pH increase retards the rate of hydrolysis. If this is the reason, the deviation should be more pronounced at lower initial borohydride concentrations where a larger fraction of the borohydride concentration is hydrolyzed. Figure S 6 (a), (c) and (e) show that no clear trend of the deviations with respect to borohydride concentration is discernible.

If the deviation is caused by the adsorption of NH_2 , the deviation should, at similar conversions, be higher at higher initial NO_2 concentration as the conversion correlates with the concentration of NH_2 (relative to the initial NO_2 concentration). Figure S 6 (b), (d), and (f) show that this is the case with only one exception.

The analysis of the deviation between fit and experiment indicates that the deviation is caused by the adsorption of NH_2 . Unfortunately, no direct proof for notable adsorption of NH_2 compared to NO_2 was found in the literature. To our best knowledge, no studies comparing the adsorption energies of NO_2 and NH_2 exist for silver. However, some findings on the other coinage metals copper and gold support the possibility. In a DFT study, Simpson et al. investigated the adsorption of trisubstituted benzene derivatives on copper(111).⁶ Here, the binding energies of 1,3,5-trinitrobenzene and 1,3,5-triaminobenzene were found to be $\Delta E_{bond} = -141.0$ and $-219.3\text{ kJ mol}^{-1}$, respectively. In a mechanistic investigation of the reduction of nitrobenzene on gold, Corma et al. found aniline as an adsorbed species on the catalyst surface during the reaction via infrared spectrometry.⁷ The kinetic investigations by Gu et al. found an adsorption constant for 4-hydroxylaminophenol much higher than the one of NO_2 .^{3,8} As the molecules are similar, it is not unrealistic that the adsorption constant of NH_2 on silver is large enough to cause significant adsorption as well. Hence, the kinetic model including the adsorption of NH_2 was applied and discussed in the main text.

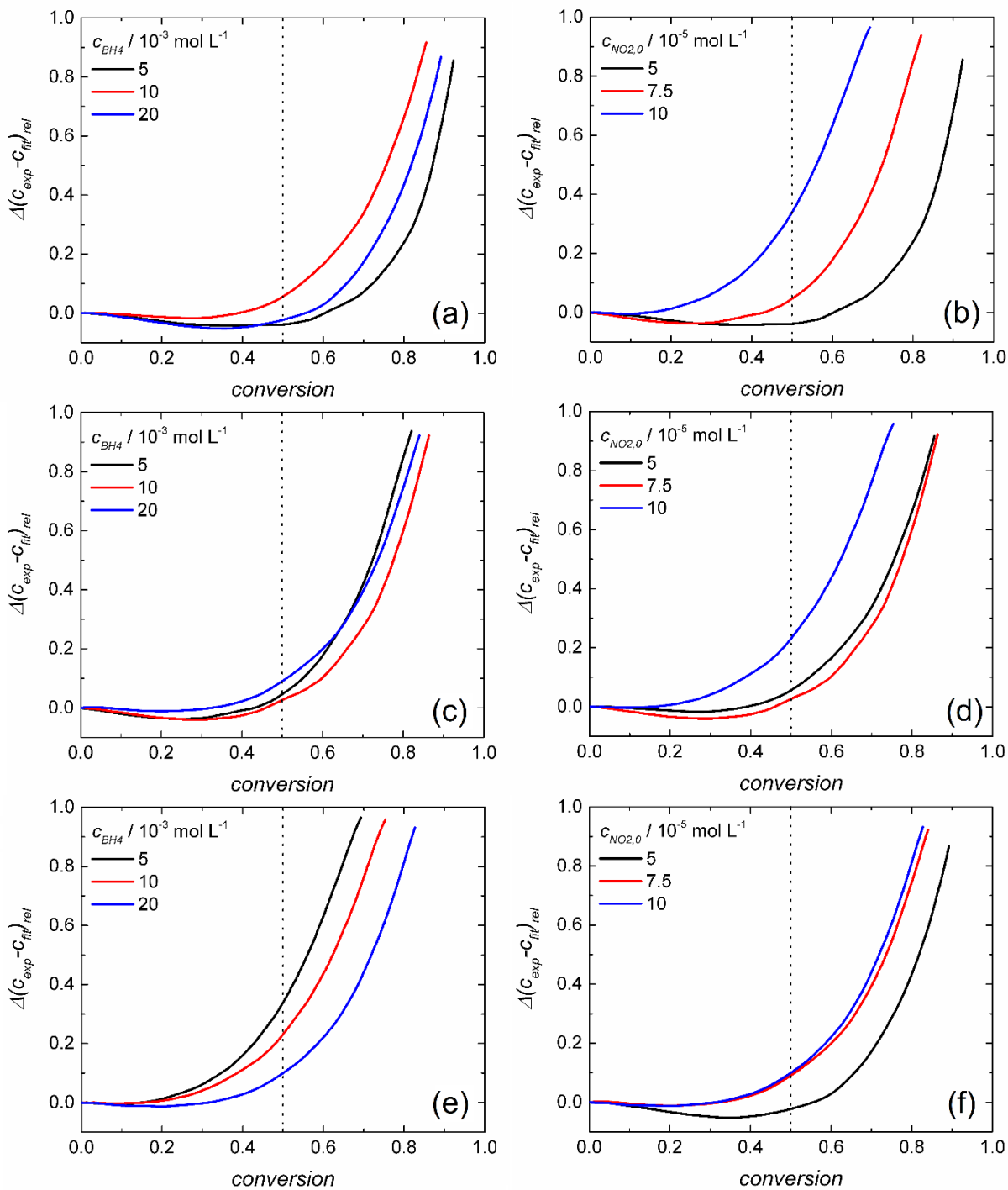


Figure S 6. Relative deviation of fitted and experimental NO_2 concentration as function of conversion. Effect of increasing borohydride concentration at $c_{\text{NO}_2} = 5 \times 10^{-5}$ (a), 7.5×10^{-5} (c) and $1 \times 10^{-4} \text{ mol L}^{-1}$ (e) and effect of increasing NO_2 concentration at $c_{\text{BH}_4} = 5 \times 10^{-3}$ (b), 1×10^{-2} (d) and $2 \times 10^{-2} \text{ mol L}^{-1}$ (f). The dotted lines indicate the transition between the fitted regime and extrapolation of the fit results to higher conversions.

Derivation of partitioning coefficients via adsorption constants of borohydride and NH_2

The data of K_{ad',BH_4} , K_{ad',NH_2} and K_{ad',NO_2} in Figures 8 (c) and (d) and Figure 9 are further analyzed with the values for the adsorption constants of borohydride K_{ad,BH_4} and NO_2 K_{ad,NO_2} , previously derived on gold nanoparticles.³ These values were obtained on nanoparticles, immobilized on spherical polyelectrolyte particles, i.e. without a PNIPAM hydrogel. Accordingly, the values are not influenced by partitioning coefficients. For NH_2 , the values for the partitioning coefficient of NO_2 are applied as the molecules are similar and no values for NH_2 exist (i.e. $K_{ad,NO_2} = K_{ad,NH_2}$). Transferring the adsorption constants obtained on gold to silver may not be an ideal solution, however, the respective values for silver can be expected to be of the same order of magnitude and, hence, provide a basis for at least a qualitative interpretation. The adsorption constants are calculated with the enthalpy and entropy of adsorption for borohydride and NO_2 ($\Delta H_{BH_4} = 37 \text{ kJ mol}^{-1}$, $\Delta S_{BH_4} = 158 \text{ J mol}^{-1} \text{ K}^{-1}$, $\Delta H_{NO_2} = 24 \text{ kJ mol}^{-1}$, $\Delta S_{NO_2} = 150 \text{ J mol}^{-1} \text{ K}^{-1}$)³ with (the Van't Hoff) equation (13) in the main text to obtain the required values between $T = 10$ and $50 \text{ }^\circ\text{C}$, given in Table S 1. The partitioning coefficients are then derived with equation (15) in the main text (i.e. $K_{part,i} = K_{ad',i}/K_{ad,i}$).

Table S 1. Parameters for the adsorption constants of borohydride, NO_2 and NH_2 , applied for the calculation of their partitioning coefficients, and resulting partitioning coefficients.

$T / ^\circ\text{C}$	$K_{ad,BH_4} / \text{L mol}^{-1}$	$K_{ad,NH_2} / \text{L mol}^{-1}$	$K_{ad,NO_2} / \text{L mol}^{-1}$	K_{part,BH_4}	K_{part,NH_2}	K_{part,NO_2}
10	29.6	2.68×10^3	2.68×10^3	1.25	6.26	6.12
15	38.8	3.20×10^3	3.20×10^3	0.983	5.16	4.93
20	50.4	3.80×10^3	3.80×10^3	0.709	5.15	3.93
25	64.8	4.47×10^3	4.47×10^3	0.536	4.70	3.24
30	82.8	5.24×10^3	5.24×10^3	0.376	4.90	2.67
35	105	6.11×10^3	6.11×10^3	0.275	5.01	2.29
40	132	7.10×10^3	7.10×10^3	0.233	3.83	1.92
45	165	8.20×10^3	8.20×10^3	0.215	2.74	1.55
50	204	9.42×10^3	9.42×10^3	0.228	2.08	0.99

References

- (1) Greenwood, N. N.; Earnshaw, A. *Chemie Der Elemente*; Wiley-VCH: Weinheim, 1988.
- (2) Wunder, S.; Lu, Y.; Albrecht, M.; Ballauff, M. Catalytic Activity of Faceted Gold Nanoparticles Studied by a Model Reaction: Evidence for Substrate-Induced Surface Restructuring. *ACS Catal.* **2011**, *1*, 908–916.
- (3) Gu, S.; Wunder, S.; Lu, Y.; Ballauff, M.; Fenger, R.; Rademann, K.; Jaquet, B.; Zacccone, A. Kinetic Analysis of the Catalytic Reduction of 4-Nitrophenol by Metallic Nanoparticles. *J. Phys. Chem. C* **2014**, *118*, 18618–18625.
- (4) Mitchell, M. *An Introduction to Genetic Algorithms*; MIT press: Cambridge, MA, 1998.
- (5) Retnamma, R.; Novais, A. Q.; Rangel, C. M. Kinetics of Hydrolysis of Sodium Borohydride for Hydrogen Production in Fuel Cell Applications: A Review. *Int. J. Hydrog. Energ.* **2011**, *36*, 9772–9790.
- (6) Simpson, S.; Zurek, E. Substituted Benzene Derivatives on the Cu(111) Surface. *J. Phys. Chem. C* **2012**, *116*, 12636–12643.
- (7) Corma, A.; Concepción, P.; Serna, P. A Different Reaction Pathway for the Reduction of Aromatic Nitro Compounds on Gold Catalysts. *Angew. Chem. Int. Ed.* **2007**, *46*, 7266–7269.
- (8) Gu, S.; Kaiser, J.; Marzun, G.; Ott, A.; Lu, Y.; Ballauff, M.; Zacccone, A.; Barcikowski, S.; Wagener, P. Ligand-Free Gold Nanoparticles as a Reference Material for Kinetic Modelling of Catalytic Reduction of 4-Nitrophenol. *Catal. Lett.* **2015**, *145*, 1105–1112.